J. Fluid Mech. (2013), *vol.* 724, *pp.* 203–233. © Cambridge University Press 2013
doi:10.1017/jfm.2013.163

Reduced-order unsteady aerodynamic models at low Reynolds numbers

Steven L. Brunton[1],†, Clarence W. Rowley[1] and David R. Williams[2]

[1]Department of Mechanical and Aerospace Engineering, Princeton University, Princeton, NJ 08544, USA

[2]Department of Mechanical, Materials, and Aerospace Engineering, Illinois Institute of Technology, Chicago, IL 60616, USA

(Received 17 October 2012; revised 4 February 2013; accepted 20 March 2013; first published online 29 April 2013)

In this paper we develop reduced-order models for the unsteady lift on a pitching and plunging aerofoil over a range of angles of attack. In particular, we analyse the pitching and plunging dynamics for two cases: a two-dimensional flat plate at $Re = 100$ using high-fidelity direct numerical simulations and a three-dimensional NACA 0006 aerofoil at $Re = 65\,000$ using wind-tunnel measurements. Models are obtained at various angles of attack and they are verified against measurements using frequency response plots and large-amplitude manoeuvres. These models provide a low-dimensional balanced representation of the relevant unsteady fluid dynamics. In simulations, flow structures are visualized using finite-time Lyapunov exponents. A number of phenomenological trends are observed, both in the data and in the models. As the base angle of attack increases, the boundary layer begins to separate, resulting in a decreased quasi-steady lift coefficient slope and a delayed relaxation to steady state at low frequencies. This extends the low-frequency range of motions that excite unsteady effects, meaning that the quasi-steady approximation is not valid until lower frequencies than are predicted by Theodorsen's classical inviscid model. In addition, at small angles of attack, the lift coefficient rises to the steady-state value after a step in angle, while at larger angles of attack, the lift coefficient relaxes down to the steady-state after an initially high lift state. Flow visualization indicates that this coincides with the formation and convection of vortices at the leading edge and trailing edge. As the angle of attack approaches the critical angle for vortex shedding, the poles and zeros of the model approach the imaginary axis in the complex plane, and some zeros cross into the right half plane. This has significant implications for active flow control, which are discussed. These trends are observed in both simulations and wind-tunnel data.

Key words: aerodynamics, flow control, low-dimensional models

1. Introduction

The unsteady aerodynamics of small-scale wings at a high angle of attack is at the focus of efforts to study bird and insect flight as well as to develop advanced controllers for high-performance micro aerial vehicles (MAVs). The short time scales

† Email address for correspondence: sbrunton@princeton.edu

https://doi.org/10.1017/jfm.2013.163 Published online by Cambridge University Press

involved in gusts and agile manoeuvres make small wings susceptible to unsteady laminar separation, which can either enhance or destroy the lift depending on the specific manoeuvre. For example, certain insects (Birch & Dickinson 2001; Zbikowski 2002; Sane 2003; Wang 2005) and birds (Videler, Samhuis & Povel 2004) use the shape and motion of their wings to maintain the high transient lift from a rapid pitch-up, while avoiding stall and the substantially decreased lift that follows. The enhanced performance observed in bio-locomotion relies on unsteady mechanisms that will be important for model-based control of MAVs (Zbikowski 2002; Pines & Bohorquez 2006). The overarching goal of this analysis is to gain an understanding of the underlying unsteady flow physics of pitching and plunging aerofoils and to develop tractable reduced-order models suitable for feedback control.

The most important parameter for quantifying the trend towards smaller, slower vehicles is the dimensionless Reynolds number, $Re = cU_\infty/\nu$, where c is the chord length of the wing, U_∞ is the free stream velocity and ν is the kinematic fluid viscosity. Small, lightweight vehicles typically experience low Reynolds number, both because of shorter wing chord length and because lighter weight leads to a lower stall velocity. Flow over an aerofoil at low Reynolds number is characterized by a thick laminar boundary layer that may have a stable separation bubble for moderate angles of attack. The effect of Reynolds number and aspect ratio on stationary small wings is discussed in Torres & Mueller (2004) and Kaplan, Altman & Ol (2007).

Unsteady aerodynamic forces are readily excited for small vehicles at low Reynolds numbers, in response to a gust disturbance, aggressive manoeuvring or high-frequency wing motion. The non-dimensional parameters governing unsteadiness in the flow over a pitching and plunging rigid aerofoil are the Strouhal number and the reduced frequency. The Strouhal number is given by $St = fA/U_\infty$, where f is the frequency of oscillation and A is the peak-to-peak amplitude of the aerofoil motion. Triantafyllou, Triantafyllou & Grosenbaugh (1993) and Anderson *et al.* (1998) demonstrated that for a pitching or plunging aerofoil, the Strouhal number is typically in the range of 0.25–0.35 for efficient propulsion, although aspect ratio has been shown to play a significant role (Buchholz & Smits 2008; Green & Smits 2008). The reduced frequency, $k = \pi fc/U_\infty$, is frequency non-dimensionalized by chord length. Both non-dimensional frequencies increase with higher frequency oscillations and smaller free-stream velocities, and they both decrease with smaller wing size. Reduced frequency unsteadiness is excited by very rapid manoeuvres, regardless of amplitude, while Strouhal number unsteadiness is excited by a combination of fast and large motion.

Flight dynamic time scales are shorter for MAVs than for traditional aircraft, because MAVs are lighter and more compact. Therefore, smaller vehicles are able to perform aggressive manoeuvres without the body inertia attenuating the motion, as is the case for large aircraft. As flight dynamic and aerodynamic time scales become comparable, it is more difficult to simultaneously meet various control objectives. This highlights the need for accurate low-order models that are compatible with both flight dynamic models and with modern, robust feedback control techniques.

Ahuja & Rowley (2010) demonstrated that the flow past a stationary flat plate, with 2 % thickness at $Re = 100$, undergoes a supercritical Hopf bifurcation at a critical angle of attack, $\alpha_c \approx 27^\circ$. Above this angle, the flow is characterized by periodic, laminar vortex shedding. They go on to develop feedback controllers, based on balanced proper orthogonal decomposition (BPOD) models (Rowley 2005), to suppress vortex shedding at large angles of attack; their actuation is a localized body force near the trailing edge and the sensors measure velocity at two locations in the near-wake.

https://doi.org/10.1017/jfm.2013.163 Published online by Cambridge University Press

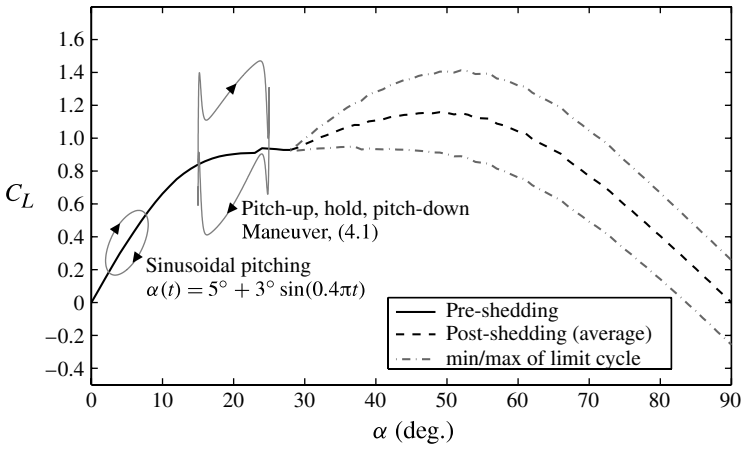


FIGURE 1. Lift coefficient, C_L, against the static angle of attack, α. The flow undergoes a Hopf bifurcation at $\alpha_c \approx 28°$. Unsteady aerofoil motion causes deviations from the static lift curve.

Figure 1 shows the lift coefficient, C_L, against a static angle of attack, α, at the same Reynolds number ($Re = 100$) for a flat plate with 1 % thickness; in this case the Hopf bifurcation occurs at $\alpha_c \approx 28°$. If the angle of attack varies in time, the lift coefficient may deviate significantly from the static lift curve, as seen by the sinusoidal pitching and pitch-up, hold, pitch-down manoeuvres. The deviation is caused by transient forces, including unsteady viscous effects, which are especially important at low Reynolds numbers, and large added-mass forces, which are given by the rate-of-work supplied to accelerate fluid out of the way of an accelerating body (Daniel 1984).

In this work, we build on the ideas in Ahuja & Rowley (2010) by using direct lift measurements and actuating the position of the wing. In keeping with the wind-tunnel perspective, including limited actuator and sensor capability, we do not make use of any linear or adjoint simulations. Instead, we construct manoeuvres that are designed to excite linear unsteady phenomena in the full nonlinear system, and obtain reduced-order models using the eigensystem realization algorithm (ERA) of Juang & Pappa (1985). Ma, Ahuja & Rowley (2011) have recently shown that the resulting models are equivalent to BPOD models, but without the need for adjoint simulations.

We develop a reduced-order modelling framework to obtain models for the unsteady aerodynamics of pitching and plunging aerofoils at various angles of attack. The models are linearized about a particular flow configuration, determined by the angle of attack, wing shape and Reynolds number, resulting in a hierarchy of models over a range of parameters. A family of aggressive pseudo-random aerofoil manoeuvres is devised to identify models from wind-tunnel measurements. Special care must be taken, since obtaining large reduced frequencies in a wind tunnel commonly involves decreased flow speeds and subsequently reduced signal-to-noise ratio measurements. The models obtained are low-dimensional, state-space representations that are ideal for use with modern robust and optimal control techniques, which will be particularly important when flight dynamic and aerodynamic time scales are comparable. Models are developed for $Re = 100$ flow past a two-dimensional flat plate and for $Re = 65\,000$ flow past a NACA 0006 aerofoil.

https://doi.org/10.1017/jfm.2013.163 Published online by Cambridge University Press

The unsteady lift data, and the resulting models, are then used to analyse properties of the unsteady flow field up to large angles of attack. In particular, models are tested over a range of reduced frequencies and angles of attack, including large amplitude, massively separated flows. The numerical results in this paper are visualized using finite-time Lyapunov exponent (FTLE) fields (Haller 2002; Shadden, Lekien & Marsden 2005). FTLE methods have been used to study low-Reynolds-number aquatic propulsion (Peng & Dabiri 2008; Wilson *et al.* 2009; Green, Rowley & Smits 2011), as well as three-dimensional turbulence (Green, Rowley & Haller 2007) and general vortex phenomena (Franco *et al.* 2007; Shadden *et al.* 2007). Lagrangian methods, such as FTLE, are particularly useful for identifying separated flows (Haller 2004; Surana, Grunberg & Haller 2006; Weldon *et al.* 2008). In this work, we use FTLE fields to infer lift mechanisms based on unsteady separated flows.

2. Classical unsteady aerodynamic models

The classical models of Wagner (1925) and Theodorsen (1935), and their variants (von Kármán & Sears 1938), remain widely used (Pullin & Wang 2004), and they provide inspiration for the state-space models in this paper as well as a benchmark to compare against. Theodorsen's model extends the quasi-steady thin aerofoil theory to include added-mass forces and the effect of idealized wake vorticity on the circulation around the aerofoil. The model assumes purely harmonic input motion of the angle of attack α and the vertical position h, so that $\alpha(t) = \mathrm{Re}(\tilde{\alpha}(t))$ and $h(t) = \mathrm{Re}(\tilde{h}(t))$, where $\tilde{\alpha}(t) = \bar{\alpha}\mathrm{e}^{\mathrm{i}\omega t}$ and $\tilde{h}(t) = \bar{h}\mathrm{e}^{\mathrm{i}\omega t}$, respectively. Defining the lift coefficient $C_L = 2L/\rho U_\infty^2 S$, where L is lift, ρ is the fluid density, U_∞ is the free-stream velocity and S is the wing area (or the chord for a two-dimensional aerofoil), Theodorsen's model is given by $C_L = \mathrm{Re}(\tilde{C}_L)$, where $\tilde{C}_L$ is

$$\tilde{C}_L = \underbrace{\frac{\pi}{2}[\ddot{\tilde{h}} + \dot{\tilde{\alpha}} - a\ddot{\tilde{\alpha}}]}_{\textit{added-mass}} + \underbrace{2\pi\left[\tilde{\alpha} + \dot{\tilde{h}} + \dot{\tilde{\alpha}}\left(\frac{1}{4} - a\right)\right]}_{\textit{quasi-steady}} C(k). \tag{2.1}$$

Here $C(k)$ is the complex-valued Theodorsen's lift deficiency function, describing the attenuation of circulation around the aerofoil by previously shed wake vorticity, in terms of the reduced frequency, $k = \omega c/2U_\infty$. Length is non-dimensionalized by the chord length c and velocity is non-dimensionalized by U_∞, the free-stream velocity. The pitch-axis location a is measured with respect to the $1/2$ chord ($a = -1/2$ is the leading edge and $a = 1/2$ is the trailing edge). Extensions of Theodorsen's model have been developed for time-domain analysis of arbitrary manoeuvres (Edwards 1977; Brunton & Rowley 2013).

The form of Theodorsen's model, composed of physically motivated terms, is particularly attractive. However, Theodorsen's model is inviscid and assumes infinitesimal motion of the aerofoil, resulting in a planar wake. These assumptions are not valid for low-Reynolds-number flows with thick, laminar boundary layers that may have significant separation and complex wake structures.

Wagner's model is formulated in the time domain by a convolution integral and it is functionally equivalent to Theodorsen's model. This is the first of a set of general indicial response models, based on analytic, numerical or experimental step-response data (Truong & Tobak 1990; Lesieutre, Reisenthel & Dillenius 1994). A general indicial response model for the circulatory lift in response to an arbitrary pitch

https://doi.org/10.1017/jfm.2013.163 Published online by Cambridge University Press

motion, $\alpha(t)$, is given by

$$C_L^{circ}(t) = \phi(t)\alpha(0^-) + \int_0^t \phi(t-\tau)\dot{\alpha}(\tau)\,\mathrm{d}\tau \tag{2.2}$$

where the 'indicial response' $\phi(t)$ is the response of the lift coefficient given a step in the angle of attack. Although this model can be quite accurate, the convolution integral formulation has two major drawbacks: first, the model is not in a state-space form that allows for modern analysis and robust control design; and, second, the contributions of various force terms are all lumped into the indicial response ϕ, making parameterization difficult.

The strengths and weaknesses of the above methods motivate the reduced-order models presented in the following section. In particular, we present a framework for obtaining low-dimensional state-space models from either theoretical, numerical or experimental lift measurements that retain many of the desirable features of the models above.

3. State-space unsteady aerodynamic models

This section presents reduced-order models for the discrete Navier–Stokes (NS) equations with moving aerofoil boundary conditions and lift force output equation, linearized about an equilibrium state. Model reduction yields low-dimensional, state-space representations of the unsteady lift coefficient, C_L, in response to pitching and plunging aerofoil motion. The resulting models are accurate for a specific wing shape, configuration and Reynolds number, and they may be built from direct numerical simulation (DNS) or experimental data.

Consider the general, nonlinear unsteady aerodynamic system arising from the unsteady NS equations, written in the general form

$$\dot{\boldsymbol{x}}_a = \boldsymbol{f}(\boldsymbol{x}_a, \boldsymbol{u}; \boldsymbol{\mu}) \tag{3.1a}$$

$$\boldsymbol{y} = \boldsymbol{g}(\boldsymbol{x}_a, \boldsymbol{u}; \boldsymbol{\mu}), \tag{3.1b}$$

where $\boldsymbol{x}_a \in \mathbb{R}^n$ contains relevant information about the aerodynamic state (vorticity or velocity field, angle of attack, amount of separation, etc.), $\boldsymbol{u} \in \mathbb{R}^p$ contains the inputs to the system (wing kinematics, actuators, etc.), $\boldsymbol{y} \in \mathbb{R}^q$ are the outputs of interest (forces, moments, pressure, etc.) and $\boldsymbol{\mu} \in \mathbb{R}^k$ are parameters (e.g. Reynolds number). The function $\boldsymbol{f}$ is related to the nonlinear NS equations, for example as the discretized equations from a fluid solver or the equations resulting from Galerkin projection onto a set of basis functions.

3.1. *Linearized pitch and plunge models*

For a model of the unsteady lift coefficient, C_L, in response to pitching motion, a general state $\boldsymbol{x}_a$ will include the fluid state $\boldsymbol{x}$ (e.g. the vorticity $\boldsymbol{\omega}$ or velocity $\boldsymbol{v}$ at grid points), as well as the angle of attack α, its rate of change $\dot{\alpha}$ and the angular acceleration $\ddot{\alpha}$, resulting in a model of the form

$$\dot{\boldsymbol{x}}_a \triangleq \frac{\mathrm{d}}{\mathrm{d}t}\begin{bmatrix}\boldsymbol{x}\\ \alpha\\ \dot{\alpha}\end{bmatrix} = \begin{bmatrix}\boldsymbol{f}_{NS}(\boldsymbol{x}, \alpha, \dot{\alpha}, \ddot{\alpha})\\ \dot{\alpha}\\ \ddot{\alpha}\end{bmatrix} \tag{3.2a}$$

$$\begin{aligned} C_L &= g_{lift}(\boldsymbol{x}, \alpha, \dot{\alpha}, \ddot{\alpha}) \\ &= g_v(\boldsymbol{x}, \alpha, \dot{\alpha}) + g_\phi(\dot{\alpha}, \ddot{\alpha}), \end{aligned} \tag{3.2b}$$

https://doi.org/10.1017/jfm.2013.163 Published online by Cambridge University Press

where $\boldsymbol{f}_{NS}$ are the discretized NS equations. The output is split into viscous forces g_v and added-mass forces g_ϕ, which depend linearly on $\dot{\alpha}$ and $\ddot{\alpha}$ (Brennen 1982). The input to (3.1) could also be vertical plunging motion $\ddot{h}$ or horizontal surging motion $\ddot{g}$.

Linearizing (3.2) about an equilibrium flow $\bar{\boldsymbol{x}}(\alpha_0)$ at a base angle of attack $\alpha_0 < \alpha_c$ yields a model for the lift coefficient C_L in response to pitch motion $\ddot{\alpha}$:

$$\frac{\mathrm{d}}{\mathrm{d}t}\begin{bmatrix}\boldsymbol{x}\\ \alpha\\ \dot{\alpha}\end{bmatrix} = \begin{bmatrix}\boldsymbol{A} & \boldsymbol{B}_1 & \boldsymbol{B}_2\\ \boldsymbol{0} & 0 & 1\\ \boldsymbol{0} & 0 & 0\end{bmatrix}\begin{bmatrix}\boldsymbol{x}\\ \alpha\\ \dot{\alpha}\end{bmatrix} + \begin{bmatrix}\boldsymbol{B}_3\\ 0\\ 1\end{bmatrix}\ddot{\alpha} \tag{3.3a}$$

$$C_L = \begin{bmatrix}\boldsymbol{C} & C_\alpha & C_{\dot{\alpha}}\end{bmatrix}\begin{bmatrix}\boldsymbol{x}\\ \alpha\\ \dot{\alpha}\end{bmatrix} + C_{\ddot{\alpha}}\ddot{\alpha}, \tag{3.3b}$$

where $\boldsymbol{A} = \partial \boldsymbol{f}_{NS}/\partial \boldsymbol{x}$, $\boldsymbol{B}_1 = \partial \boldsymbol{f}_{NS}/\partial \alpha$, $\boldsymbol{B}_2 = \partial \boldsymbol{f}_{NS}/\partial \dot{\alpha}$, $\boldsymbol{B}_3 = \partial \boldsymbol{f}_{NS}/\partial \ddot{\alpha}$, $\boldsymbol{C} = \partial g_v/\partial \boldsymbol{x}$, $C_\alpha = \partial g_v/\partial \alpha$, $C_{\dot{\alpha}} = \partial(g_v + g_\phi)/\partial \dot{\alpha}$ and $C_{\ddot{\alpha}} = \partial g_\phi/\partial \ddot{\alpha}$. It is important to note that (3.3) is linearized about an equilibrium flow state $\bar{\boldsymbol{x}}(\alpha_0)$ at a base angle of attack α_0 for pitching about a fixed pitch-axis location a. Theodorsen's lift model has recently been cast into the state-space form (3.3) in Brunton & Rowley (2013).

The model in (3.3) is in a general form with no assumption made about the fluid state $\boldsymbol{x}$. However, we may assume that the fluid state $\boldsymbol{x}$ represents vorticity and that the flow responds instantaneously to pitch acceleration $\ddot{\alpha}$ with an unsteady (irrotational) potential flow, resulting in the added-mass forces $C_{\dot{\alpha}}\dot{\alpha}$ and $C_{\ddot{\alpha}}\ddot{\alpha}$. Therefore, $\boldsymbol{B}_3 = \boldsymbol{0}$, so that $\dot{\alpha}$ is the input to the transient fluid dynamics in $\boldsymbol{x}$. We may further simplify the model by defining a new state variable $\tilde{\boldsymbol{x}} = \boldsymbol{x} + \boldsymbol{A}^{-1}\boldsymbol{B}_1\alpha$; $\boldsymbol{A}$ is invertible for the linearized NS equations away from bifurcation points ($\alpha_{crit} \approx 28^\circ$ for a plate at $Re = 100$). Writing $\boldsymbol{B}_{\dot{\alpha}} = \boldsymbol{B}_2 + \boldsymbol{A}^{-1}\boldsymbol{B}_1$, the model (3.3) then takes the form

$$\frac{\mathrm{d}}{\mathrm{d}t}\begin{bmatrix}\tilde{\boldsymbol{x}}\\ \alpha\\ \dot{\alpha}\end{bmatrix} = \begin{bmatrix}\boldsymbol{A} & \boldsymbol{0} & \boldsymbol{B}_{\dot{\alpha}}\\ \boldsymbol{0} & 0 & 1\\ \boldsymbol{0} & 0 & 0\end{bmatrix}\begin{bmatrix}\tilde{\boldsymbol{x}}\\ \alpha\\ \dot{\alpha}\end{bmatrix} + \begin{bmatrix}\boldsymbol{0}\\ 0\\ 1\end{bmatrix}\ddot{\alpha} \tag{3.4a}$$

$$C_L = \begin{bmatrix}\boldsymbol{C} & C_\alpha - \boldsymbol{C}\boldsymbol{A}^{-1}\boldsymbol{B}_1 & C_{\dot{\alpha}}\end{bmatrix}\begin{bmatrix}\tilde{\boldsymbol{x}}\\ \alpha\\ \dot{\alpha}\end{bmatrix} + C_{\ddot{\alpha}}\ddot{\alpha}. \tag{3.4b}$$

The term $\boldsymbol{C}\boldsymbol{A}^{-1}\boldsymbol{B}_1$ must be equal to zero, since the C_α term accounts for all of the lift in the absence of wing motion, regardless of the choice of coordinates for $\boldsymbol{x}$. In (3.4), the wing motion $(\alpha, \dot{\alpha}, \ddot{\alpha})$ enters the transient fluid dynamic state $\tilde{\boldsymbol{x}}$ through the $B_{\dot{\alpha}}$ term. It is possible to write an equivalent model by introducing another change of coordinates, $\tilde{\tilde{\boldsymbol{x}}} = \tilde{\boldsymbol{x}} + \boldsymbol{A}^{-1}\boldsymbol{B}_{\dot{\alpha}}\dot{\alpha}$, and $\boldsymbol{B}_{\ddot{\alpha}} = \boldsymbol{A}^{-1}B_{\dot{\alpha}}$. The resulting model is

$$\frac{\mathrm{d}}{\mathrm{d}t}\begin{bmatrix}\tilde{\tilde{\boldsymbol{x}}}\\ \alpha\\ \dot{\alpha}\end{bmatrix} = \begin{bmatrix}\boldsymbol{A} & \boldsymbol{0} & \boldsymbol{0}\\ \boldsymbol{0} & 0 & 1\\ \boldsymbol{0} & 0 & 0\end{bmatrix}\begin{bmatrix}\tilde{\tilde{\boldsymbol{x}}}\\ \alpha\\ \dot{\alpha}\end{bmatrix} + \begin{bmatrix}\boldsymbol{B}_{\ddot{\alpha}}\\ 0\\ 1\end{bmatrix}\ddot{\alpha} \tag{3.5a}$$

$$C_L = \begin{bmatrix}\boldsymbol{C} & C_\alpha & C_{\dot{\alpha}} - \boldsymbol{C}\boldsymbol{A}^{-1}\boldsymbol{B}_{\dot{\alpha}}\end{bmatrix}\begin{bmatrix}\tilde{\tilde{\boldsymbol{x}}}\\ \alpha\\ \dot{\alpha}\end{bmatrix} + C_{\ddot{\alpha}}\ddot{\alpha}. \tag{3.5b}$$

https://doi.org/10.1017/jfm.2013.163 Published online by Cambridge University Press

We may generalize the above model to include pitch, plunge or combined pitch and plunge motions. The general model is given by

$$\frac{\mathrm{d}}{\mathrm{d}t}\begin{bmatrix}\boldsymbol{x}\\ \boldsymbol{u}\\ \dot{\boldsymbol{u}}\end{bmatrix} = \begin{bmatrix}\boldsymbol{A} & \boldsymbol{0} & \boldsymbol{0}\\ \boldsymbol{0} & \boldsymbol{0} & \boldsymbol{I}\\ \boldsymbol{0} & \boldsymbol{0} & \boldsymbol{0}\end{bmatrix}\begin{bmatrix}\boldsymbol{x}\\ \boldsymbol{u}\\ \dot{\boldsymbol{u}}\end{bmatrix} + \begin{bmatrix}\boldsymbol{B}_{\ddot{u}}\\ \boldsymbol{0}\\ \boldsymbol{I}\end{bmatrix}\ddot{\boldsymbol{u}} \tag{3.6a}$$

$$\boldsymbol{y} = [\boldsymbol{C} \quad \boldsymbol{C}_u \quad \boldsymbol{C}_{\dot{u}}]\begin{bmatrix}\boldsymbol{x}\\ \boldsymbol{u}\\ \dot{\boldsymbol{u}}\end{bmatrix} + \boldsymbol{C}_{\ddot{u}}\ddot{\boldsymbol{u}}. \tag{3.6b}$$

For this paper, we use a lift coefficient output, $\boldsymbol{y} = C_L$. Pure pitch is given by $\boldsymbol{u} = \alpha$, pure plunge is given by $\boldsymbol{u} = h$ and combined pitch and plunge is given by $\boldsymbol{u} = [\alpha \quad h]^{\mathrm{T}}$. Horizontal wing motion, linearized about a nominal free-stream velocity, may be incorporated into a model of the form in (3.6), extending it to full planar wing motion. Preliminary results indicate that wing motions parallel to the plate's angle of incidence excite smaller unsteady aerodynamic forces compared with perpendicular motions, over a range of angles of attack (Brunton 2012). This suggests that horizontal plate motion, or variations in U_∞, will excite larger forces normal to the plate at larger angles of attack. From the perspective of unsteady fluid dynamics, translation of the wing in air has the same effect as uniformly gusting wind over a stationary wing.

3.2. *Reduced-order model identification*

Similar to Theodorsen's expression, the models above are written in terms of the quasi-steady and added-mass forces, given by the coefficients $C_u, C_{\dot{u}}, C_{\ddot{u}}$ in (3.6), and a model for the transient fluid dynamics, given by $(\boldsymbol{A}, \boldsymbol{B}_{\dot{u}}, \boldsymbol{C})$ in (3.4) and $(\boldsymbol{A}, \boldsymbol{B}_{\ddot{u}}, \boldsymbol{C})$ in (3.6). All of the terms in the models above depend on the specific wing geometry, configuration and Reynolds number used to determine the equilibrium flow state about which the equations are linearized. In both cases, the transient fluid dynamic models are written in terms of the vector $\boldsymbol{x} \in \mathbb{R}^n$, which is a representation of the fluid state, for example the velocity or vorticity at each grid point; typically, the dimension n is quite large.

We seek a reduced-order model, $(\boldsymbol{A}_r, \boldsymbol{B}_r, \boldsymbol{C}_r)$, of the full-state model, $(\boldsymbol{A}, \boldsymbol{B}, \boldsymbol{C})$, in terms of a low-dimensional state, $\boldsymbol{x}_r \in \mathbb{R}^r$, where $r \ll n$. This reduced-order model is obtained by first identifying and removing the coefficients $C_u, C_{\dot{u}}, C_{\ddot{u}}$ from an impulse response in either $\dot{\boldsymbol{u}}$ or $\ddot{\boldsymbol{u}}$, and identifying the remaining transient dynamics using the ERA of Juang & Pappa (1985). Identifying the quasi-steady and added-mass coefficients upfront guarantees accuracy of the model in the limit of low-frequency and high-frequency motions. The modelling effort is then targeted at the transient unsteady fluid dynamics that occurs at intermediate frequencies, allowing for a low-order model that is accurate over a range of frequencies.

Ma *et al.* (2011) demonstrated that the resulting ERA model is equivalent to a model obtained by BPOD, and therefore captures the r most observable and controllable fluid states in a balanced representation. Balanced models are ideal for efficiently and faithfully representing the input–output relationship in fluids for a particular choice of sensors and actuators (Rowley 2005; Ilak & Rowley 2008; Bagheri, Brandt & Henningson 2009; Illingworth, Morgans & Rowley 2010). Moreover, because of the relationship between ERA, BPOD and balanced truncation, there are upper and lower error bounds for the model performance at a given order in terms of the Hankel singular values (Dullerud & Paganini 2000; Rowley 2005).

https://doi.org/10.1017/jfm.2013.163 Published online by Cambridge University Press

However, there is a wealth of alternative methods for the identification of state-space models from input–output data, as in Ljung (1999).

Although the models presented here are based entirely on direct measurements of the lift coefficient, it is possible to collect additional velocity field snapshots and construct direct and pseudo-adjoint modes (Or & Speyer 2010). These modes would provide a basis for projecting the state vector from a model at one linearization point onto the state vector for another model at a different linearization point. This approach would lead to gain-scheduled or linear-parameter-varying (LPV) models (Apkarian, Pellanda & Tuan 2000; Bamieh & Giarré 2002) and this is a subject of current interest to the authors.

The reduced-order models presented in this work are obtained from an approximation of the discrete-time impulse response in either $\dot{\alpha}$ (step in α), $\ddot{\alpha}$ (step in $\dot{\alpha}$) or $\ddot{h}$ (step in vertical velocity). These responses are obtained from manoeuvres related to the canonical pitch-up, hold, pitch-down manoeuvre that was developed by Eldredge, Wang & Ol (2009) to study low-Reynolds-number separation phenomena across simulations and experiments. In the case of direct simulations, a smoothed linear ramp step is used. This manoeuvre is ideal for identifying unsteady aerodynamic models, because the unsteady contribution from the quasi-steady, added-mass and transient terms are separated in time.

For wind-tunnel measurements, we use a frequency-rich input manoeuvre in conjunction with the observer/Kalman filter identification (OKID) algorithm (Juang *et al.* 1991), which estimates the impulse response of a linear system in the presence of noisy measurements. Obtaining high reduced frequencies in a wind tunnel typically involves low free-stream flow velocity, and corresponding low signal-to-noise ratio measurements. Therefore, a pseudo-random sequence of smoothed ramp steps are concatenated to form an aggressive system identification manoeuvre. This idea is inspired by the pulsed-blowing identification of Kerstens *et al.* (2011). Because the input to this manoeuvre is a sequence of discrete impulses in $\ddot{\boldsymbol{u}}$, the model identified is of the form in (3.6).

After obtaining a discrete-time step response in either $\boldsymbol{u}$ or $\dot{\boldsymbol{u}}$, the quasi-steady and added-mass coefficients $C_{\boldsymbol{u}}$, $C_{\dot{\boldsymbol{u}}}$ and $C_{\ddot{\boldsymbol{u}}}$ are identified and subtracted from the measured response. Next, a model for the remaining transient fluid dynamics is obtained using the ERA. The transient portion $(\boldsymbol{A}, \boldsymbol{B}, \boldsymbol{C})$ of the model in (3.4) and (3.6) is approximated by the ERA model $(\boldsymbol{A}_r, \boldsymbol{B}_r, \boldsymbol{C}_r)$ of order $r \ll n = \dim(\boldsymbol{A})$; the input is either $\dot{\boldsymbol{u}}$ or $\ddot{\boldsymbol{u}}$ (for example, $\boldsymbol{u} = \alpha$ for pitch) and the output is C_L. The general procedure is summarized.

(*a*) Obtain the impulse response in either $\dot{\boldsymbol{u}}$ or $\ddot{\boldsymbol{u}}$, possibly via OKID.

(*b*) Determine $C_{\boldsymbol{u}}$, $C_{\dot{\boldsymbol{u}}}$ and $C_{\ddot{\boldsymbol{u}}}$. The coefficients $C_{\boldsymbol{u}}$ and $C_{\ddot{\boldsymbol{u}}}$ guarantee correct low-frequency and high-frequency behaviour of the model, respectively.

(*c*) Identify a reduced-order model for remaining dynamics with the ERA.

Specific details about the algorithms and manoeuvres are provided in Brunton (2012).

4. Results: two-dimensional flow past a flat plate at $Re = 100$

4.1. *Direct numerical simulation*

The numerical results in this paper are based on DNS of the incompressible two-dimensional NS equations. We use the fast multi-domain immersed boundary projection method (IBPM) of Taira & Colonius (2007) and Colonius & Taira (2008).

https://doi.org/10.1017/jfm.2013.163 Published online by Cambridge University Press

This method has been rigourously verified against standard examples, as well as a low-Reynolds-number tow-tank experiment in oil (Colonius & Taira 2008).

The immersed body is a rigid flat plate aerofoil that may either pitch or plunge with velocity $\boldsymbol{v}_B$. The boundary conditions are uniform flow in the far field, which is valid for a sufficiently large domain, and specified velocity $\boldsymbol{v}_B$ at points along the body. An efficient multi-domain approach is used, resulting in a series of nested grids, each twice as large as the previous. The Poisson equation is solved on the largest domain with zero boundary conditions, and the interpolated stream function from this larger grid is used for the boundary condition on the next smaller grid. The Poisson equation is then solved on this smaller grid and the process is repeated until the equations have been solved on all grids. Time integration is performed using the implicit Crank–Nicolson scheme for the viscous diffusion and a third-order Runge–Kutta scheme for the convective terms.

The computational domain consists of five nested grids, using the multi-domain approach above. The finest grid covers a domain of 4×4 (with lengths non-dimensionalized by chord), and the coarsest covers a domain of 64×64. Each grid has resolution of 400×400, which is sufficient for converged results at $Re = 100$. In addition, the method is slightly modified to solve the equations of motion in the body-fixed frame of the flat plate by introducing a moving baseflow with uniform and purely rotational components. In this formulation, the locations of the boundary points relative to the grid do not change in time, so that the matrix involved in solving for the boundary forces is constant and can be decomposed (e.g. by a Cholesky factorization) once at the beginning of the calculation. This approach is significantly faster than available alternatives when the boundary points move relative to the grid.

4.2. *Lagrangian particle analysis*

The FTLE field is used to visualize the unsteady flow field, because it is well suited for identifying regions of separated flow and wake structures. Ridges of the FTLE field that satisfy an additional hyperbolicity condition are Lagrangian coherent structures (LCSs) (Haller 2002; Shadden *et al.* 2005), and they are time-varying analogues of the stable and unstable manifolds from dynamical systems theory.

This analysis involves advecting passive tracer particles through the time-varying fluid velocity field by numerical integration, resulting in a particle flow map. The FTLE is the maximum singular value of the flow map Jacobian, logarithmically scaled with respect to the advection time. We use a computationally efficient method to compute the FTLE field (Brunton & Rowley 2010), whereby a flow map with long advection time is broken up into the composition of a number of intermediate flow maps with short advection time. Neighboring FTLE field computations may reuse the intermediate flow maps, which dramatically improves computational efficiency. The FTLE visualizations in this paper are obtained by integrating particles backward in time, yielding FTLE ridges that attract particles in forward time.

Figure 2 shows the attracting FTLE structures for simulated flow past a flat plate at $Re = 100$ in various configurations. Ridges in the FTLE field indicate the stable separated flow behind a stationary plate at $\alpha_0 = 25°$, the vortex shedding behind a stationary plate at $\alpha_0 = 35°$, the von Kármán vortex street behind a pitching plate and the formation of a large leading-edge vortex for a plunging plate with $\alpha_0 = 20°$ bias.

4.3. *Models linearized at* $\alpha_0 = 0°$

At zero angle of attack, ramped step-response simulations are obtained for a flat plate pitching about various points (leading edge, quarter chord and middle chord) and

https://doi.org/10.1017/jfm.2013.163 Published online by Cambridge University Press

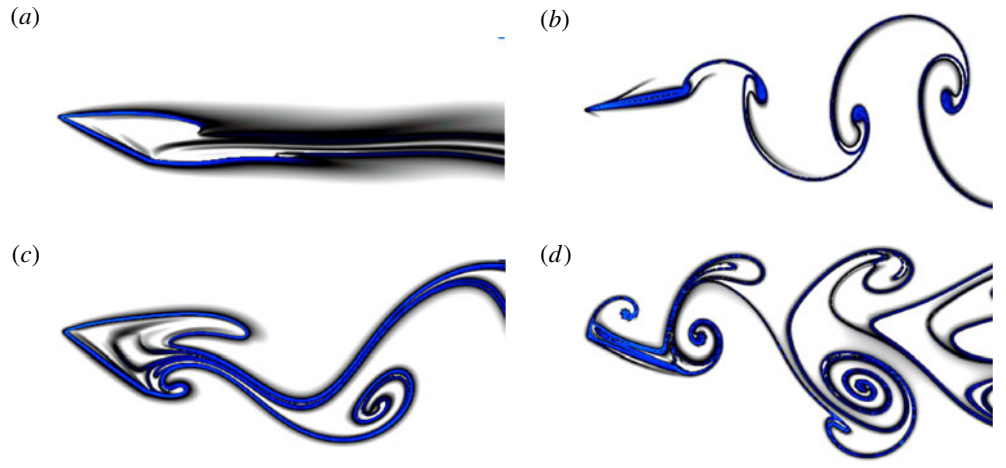


FIGURE 2. (Colour online) FTLE field for various two-dimensional separated flows: (*a*) steady flow past a flat plate at $\alpha = 25°$; (*b*) unsteady vortex shedding past a flat plate at $\alpha = 35°$; (*c*) von Kàrmàn vortex street behind a pitching plate; (*d*) leading-edge separation for a plunging plate with $\alpha = 20°$. The Reynolds number for all flows is $Re = 100$, and the reduced frequency is $k = 1.26$ for the pitching and plunging cases.

plunging vertically. The lift coefficient history from the step-response simulations are synthesized into models of the form in (3.4) for pitch and (3.6) for plunge, with ERA models $(\boldsymbol{A}_r, \boldsymbol{B}_r, \boldsymbol{C}_r)$ for the transient viscous fluid dynamics of order $r = 7$. In addition, a multiple-input model of the form in (3.6) is obtained that combines plunging with pitching about various points. For the multiple-input case of combined pitch and plunge, the ERA model also has order $r = 7$. Although a model of lower order is sufficient to capture much of the behaviour at $\alpha_0 = 0°$, a seventh-order model is necessary at larger angles of attack, as will be shown in the next section.

4.3.1. *Small-amplitude motions*

The reduced-order models presented are based on ramped step-response simulations with a small step magnitude M; $M = 0.1°$ in the case of pitching motion, and $M = 0.1°$ effective angle of attack ($\dot{h} = 0.00175$) in the case of plunging motion. Therefore, it is natural to compare the models with DNS for small-amplitude motions. The frequency response for each model is computed for sinusoidal input $u(t) = M\sin(\omega t)$ with $M = 1°$ for pitch ($u = \alpha$) and $M = 0.01$ for plunge ($u = h$). The input to the models is $\ddot{u} = -M\omega^2\sin(\omega t)$, so that the Bode plot is a frequency response from input $\ddot{u}$ to C_L.

Figure 3 shows the frequency response (i.e. Bode plot) comparing the DNS, reduced-order models (3.4) and (3.6), Theodorsen's model (2.1) and indicial response (2.2) for pitching about the quarter chord. Similar agreement is found in Bode plots for pitch about the leading edge and mid-chord as well as for plunge motion. In all of the Bode plots and step-response plots, the low-order ERA models (single-input, single-output as well as the multi-input, single-output) accurately reproduce the frequency response computed by DNS. Moreover, the ERA model is nearly identical to the indicial response model, as they are both based on the same numerical step response. Theodorsen's model consistently over predicts the quasi-steady lift slope, and is not as accurate in capturing the phase.

https://doi.org/10.1017/jfm.2013.163 Published online by Cambridge University Press

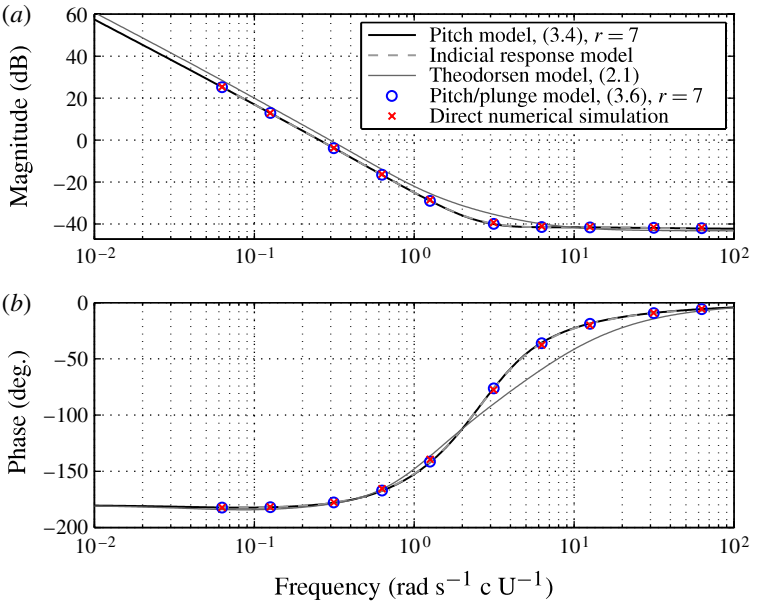


FIGURE 3. (Colour online) Frequency response of reduced-order model (3.4) (seven-mode ERA component), indicial response, Theodorsen and DNS (×) for pitching at quarter chord. The multiple-input ERA model (3.6) for pitch/plunge agrees well (circle, ○).

It is important to gain a physical intuition for the Bode plots and how they relate to the aerodynamic response. The low-frequency asymptote in each Bode plot corresponds to the quasi-steady case when the lift coefficient depends only on the angle of attack in the case of pitch, or effective angle of attack in the case of plunge. For pitching motion, the low-frequency asymptote in the magnitude plot has a slope of -40 dB/decade, where a decade is defined as an order of magnitude in frequency, and each integral of the input adds -20 dB/decade to the magnitude slope. The -40 dB/decade slope is consistent with the fact that α is obtained by integrating the input $\ddot{\alpha}$ twice. In the case of plunge, the low-frequency asymptote has a slope of -20 dB/decade, since the effective angle of attack is related to $\dot{h}$ which is the integral of the input $\ddot{h}$. In all instances, the low-frequency asymptote of the model is lower than that of Theodorsen's model, which uses the inviscid 2π lift slope and over-predicts the true lift slope at $Re = 100$. The high-frequency asymptote in the Bode magnitude plot corresponds to the case when there are large accelerations and the lift coefficient is strongly influenced by added-mass forces. In the case of pitch about the quarter chord and plunge motion, there are added-mass forces directly proportional to the inputs ($\ddot{\alpha}$ and $\ddot{h}$), so that the Bode plot has zero slope at high frequencies. These forces are captured by the $C_{\ddot{\alpha}}$ and $C_{\ddot{h}}$ terms in (3.6) and (3.4). There is no added-mass lift force proportional to $\ddot{\alpha}$ in the case of mid-chord pitching, but there are forces proportional to $\dot{\alpha}$, so the Bode plot has a slope of -20 dB/decade at high frequencies. This information is also reflected in the Bode phase plot. The phase at low-frequency starts at $-180°$ for the pitching models, which is consistent with the fact that the angle of attack is the second integral of the input (twice integrating a sinusoid results in a negative sinusoid, hence the $-180°$ phase).

https://doi.org/10.1017/jfm.2013.163 Published online by Cambridge University Press

4.4. *Models linearized at subcritical angles, $\alpha < \alpha_c$*

As the plate's angle of attack is increased, the flow physics becomes significantly more involved. Increasing the angle of attack results in an adverse pressure gradient on the upper surface that thickens the upper boundary layer until the flow reverses, resulting in a stable, attached separation bubble. Above a critical angle of attack, $\alpha_c \approx 28^\circ$, the separation bubble bursts, resulting in periodic, laminar vortex shedding.

This section presents models for a flat plate linearized at various angles of attack up to the critical angle, α_c, at which a Hopf bifurcation occurs. These cases provide a more challenging demonstration of the modelling procedure, because the transient fluid dynamic interactions are increasingly complex and important at larger angles of attack. It is observed that at $Re = 100$, a manoeuvre will have an approximately linear response if the amplitude of the manoeuvre is within $\pm 10^\circ$ of a base angle α_0, as long as the maximum excursion does not exceed α_{crit}. In these cases, a single linearized model is sufficient.

The choice of model order r is important in the following results and depends on a number of factors. First, the order should be sufficiently high so that the frequency response curves converge for all models of equal order or higher, across all frequencies. This is another way of saying that the difference between models of successive orders should be sufficiently small in the infinity norm for models of order greater than or equal to r. In addition, we are interested in capturing certain transient features of the time-domain response, including the frequency and decay rate of oscillations for large angles of attack. For larger angles of attack, we find that a model of order $r = 7$ is required to accurately capture the desired dynamics. Although the flow is less complex at low angles of attack, we use the same model order for each angle so that we may understand how branches of eigenvalues move as α_0 increases. However, we will see in § 4.4.2 that even for $\alpha_0 = 0^\circ$ there is a subtle feature of the time-response that is not captured for $r < 7$. Finally, the ERA provides balanced reduced-order models, as shown in Ma *et al.* (2011), so that we have upper and lower bounds on the error of a model for a given model order in terms of the Hankel singular values.

Although time-domain performance is necessary for these models to be predictive, an accurate time-domain response does not guarantee that the model will be accurate for feedback control design. Therefore, it is important to investigate model performance in the frequency domain. Convergence of models of successive order in the gap metric is a particularly relevant measure for control design, and this is the subject of current work.

4.4.1. *Frequency domain analysis*

Using the reduced-order modelling technique described in § 3, we have computed reduced-order models linearized at $\alpha_0 \in [0^\circ, 27^\circ]$ in 1° increments. Figure 4 shows the frequency response of models linearized at $\alpha_0 = 0^\circ$, $\alpha_0 = 10^\circ$ and $\alpha_0 = 20^\circ$, and the corresponding data from DNS. As seen in figure 1, the lift slope decreases for increasing angle of attack, so it is not surprising that the low-frequency magnitude in the Bode plot decreases for increasing angle of attack. In addition, we see that at larger angle of attack the phase converges to -180° at lower frequencies, indicating that solutions take longer to reach equilibrium in the time domain. This is consistent with the fact that for larger angles of attack the system is closer to instability, and a pair of eigenvalues of the system approach the imaginary axis, lengthening the time scale of relaxation.

https://doi.org/10.1017/jfm.2013.163 Published online by Cambridge University Press

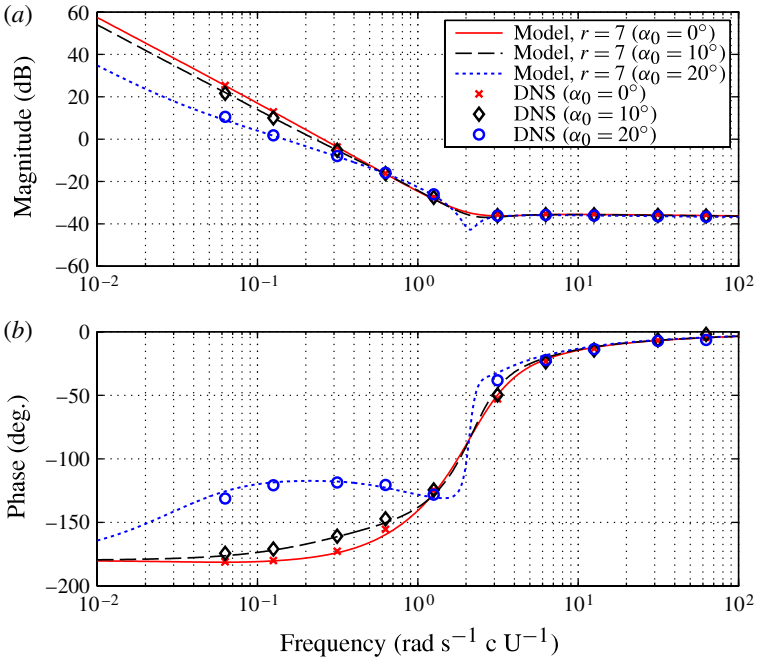


FIGURE 4. (Colour online) Frequency response of models for pure pitching about the leading edge, linearized at $\alpha_0 = 0°$, $\alpha_0 = 10°$ and $\alpha_0 = 20°$. Results from DNS linearized at $\alpha_0 = 0°$, $\alpha_0 = 10°$ and $\alpha_0 = 20°$ are included for comparison.

To see this more clearly, we plot the poles and zeros of the models for $\alpha_0 \in [0°, 27°]$, shown in figure 5. The model given by (3.4) always has two poles at the origin because the input $\ddot{\alpha}$ must be integrated twice to obtain the states $\dot{\alpha}$ and α. Because we use an ERA model of order $r = 7$ for the transient dynamics, there are seven branches of poles, in addition to the two poles at the origin; there are nine branches of zeros.

The most striking feature of figure 5 is that as angle of attack increases, a pair of poles and a pair of zeros march towards the imaginary axis. This explains the longer relaxation times (convergence of Bode plots to $-180°$ at successively lower frequencies). It also indicates that the models are capturing the dynamics as the system approaches a Hopf bifurcation. It is also interesting to note that there is a second set of poles and zeros that branch from the real axis and march toward the imaginary axis for increasing angle of attack. This is consistent with the fact that at larger angle of attack, there is more complicated limit cycle behaviour. It is not surprising that the flow may undergo several Hopf bifurcations as angle of attack or Reynolds number is increased, as observed by Ruelle & Takens (1971).

4.4.2. *Time domain analysis*

The step-response simulations for the various base angles from $\alpha_0 = 0°$ to $\alpha_0 = 27°$ are plotted in figure 6. The lift coefficient at the base angle is subtracted, and we only plot the transient dynamics after the step, so added mass is omitted. A seven-mode model is required to accurately capture the frequency and decay rate of the oscillations in the large angle of attack cases (bottom curves). A lower-order model is able to capture the general trends in the low angle of attack cases. However, a seven-mode

https://doi.org/10.1017/jfm.2013.163 Published online by Cambridge University Press

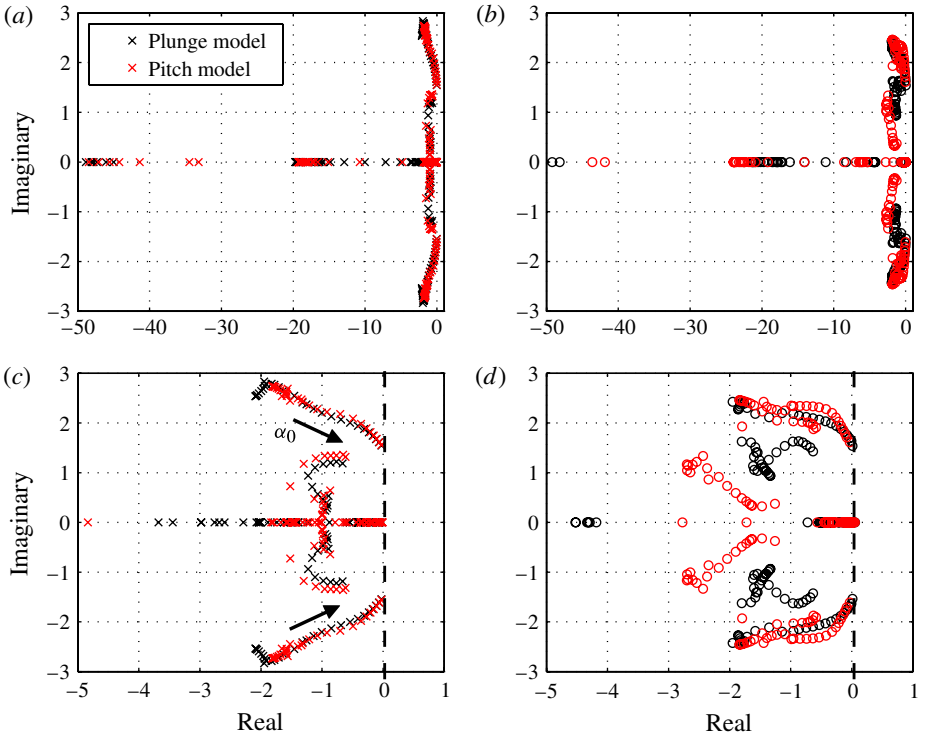


FIGURE 5. (Colour online) Poles (*a,c*, ×) and zeros (*b,d*, ○) of models for pitch about the middle-chord and plunge, linearized at various angle of attack, from $\alpha = 0°$ to $\alpha = 27°$. Enlarged views are given in (*c,d*).

model is also required to accurately capture the transient dip in the lift coefficient between one and five convective times for the $\alpha_0 = 0°$ case (top curve). It is worth noting that this data is based on a small, fast manoeuvre which yields relatively small variations in the lift coefficient. Although this works well for DNS, the lift variations are hundreds of times smaller than those of a canonical manoeuvre, shown in figure 7, and they may be too subtle for experimental measurements, motivating the aggressive manoeuvres used in the wind-tunnel analysis.

A large amplitude pitch-up, hold, pitch-down manoeuvre, developed by Eldredge *et al.* (2009) to study separation phenomena in pitching aerofoils, is given by the following:

$$\alpha(t) = \alpha_0 + \alpha_{max}\frac{G(t)}{\max(G(t))}, \quad G(t) = \log\left[\frac{\cosh(a(t-t_1))\cosh(a(t-t_4))}{\cosh(a(t-t_2))\cosh(a(t-t_3))}\right]. \quad (4.1)$$

The manoeuvre from (4.1) is used, at an angle of attack starting at $\alpha_0 = 15°$ and reaching a maximum angle of 25° before coming back down to 15°; the pitch point is the leading edge, the parameter $a = 11$ determines how sharp the corners are in the manoeuvre, and $t_1 = 1, t_2 = 3, t_3 = 4, t_4 = 6$. The parameter value $a = 11$ excites large added-mass forces and is chosen to match the value used for simulations and experiments in Ol *et al.* (2010). This manoeuvre also excites leading-edge separation, as seen in the accompanying FTLE images. The comparison of various reduced-order models with DNS is shown in figure 7. Theodorsen's model is included for a baseline comparison. The pitch model linearized about $\alpha_0 = 15°$ matches the DNS very closely,

https://doi.org/10.1017/jfm.2013.163 Published online by Cambridge University Press

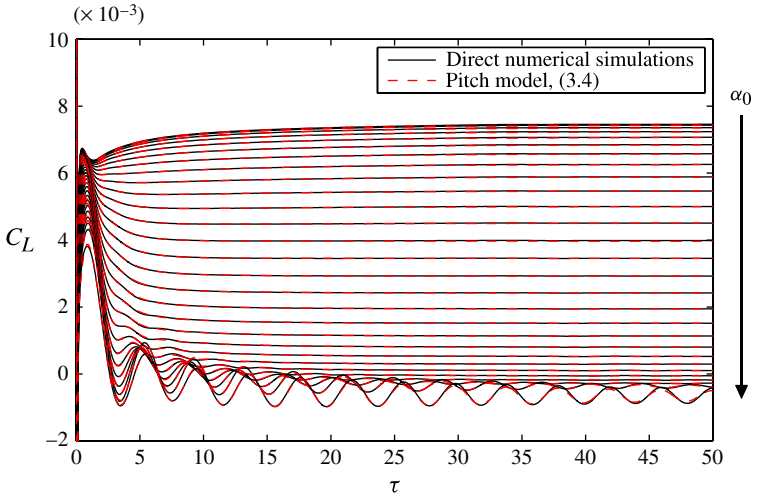


FIGURE 6. (Colour online) Simulations and model prediction for small step in pitch angle about the leading edge of magnitude $M = 0.1^\circ$ from a reference angle α_0 to $\alpha_0 + M$ for $\alpha_0 \in [0^\circ, 27^\circ]$. The initial lift coefficient $C_L(\alpha_0)$ is subtracted and α_0 increases with the arrow. ERA model order is $r = 7$. The convective time is non-dimensionalized by c and U: $\tau = tU/c$.

capturing the negative slope of the lift coefficient during the constant-angle hold period between $\tau = 3$ and $\tau = 4$; this is an important feature that is observed at large angles of attack, both in simulations and in experiments. The model linearized about $\alpha_0 = 0^\circ$ is more accurate than Theodorsen's model, but has the wrong lift coefficient slope. A model linearized at $\alpha_0 = 15^\circ$ is a natural choice since the manoeuvre begins starts at 15° with a fully developed boundary layer, so that we may view the manoeuvre as an excursion from $\alpha_0 = 15^\circ$. Since the manoeuvre ends at 15°, it would then be possible to simulate a subsequent pitch-down manoeuvre, based at $\alpha_0 = 15^\circ$.

4.5. *Behaviour at post-critical angles, $\alpha > \alpha_c$*

It is important to establish how the linear models from § 3 perform on large-amplitude manoeuvres with significant flow separation. For this reason, we consider a number of large-amplitude pitch and plunge manoeuvres and investigate both the model performance and the flow field itself.

First, consider the pitch-up, hold, pitch-down manoeuvre from 0 to 45° and back down, given by (4.1) and shown in figure 8(*a*). This manoeuvre exceeds the critical angle of attack, and as is seen in the FTLE visualization, a large leading-edge vortex forms and convects downstream. A piecewise linear model is obtained by running two models, one linearized at $\alpha_0 = 0^\circ$ and another at $\alpha_0 = 25^\circ$, and switching between the models at time $\tau = 3.0$ and again at $\tau = 4.0$; C_L is matched at the switching point so that the output is continuous. The model does surprisingly well, considering the large separated flow structures, although there is error during each phase of the manoeuvre.

There is no guarantee that a piecewise linear model will faithfully predict a generic large-amplitude pitch-up manoeuvre with a nonlinear response. However, because of the rapid nature of the pitch-up in figure 8, the boundary layer does not have time to catch up, and the lift response is surprisingly similar to the $\alpha_0 = 0^\circ$ linearized model prediction for $\tau < 3.0$. During the hold region, after the motion has stopped, we switch to our best large angle of attack model, linearized at $\alpha_0 = 25^\circ$, which yields the

https://doi.org/10.1017/jfm.2013.163 Published online by Cambridge University Press

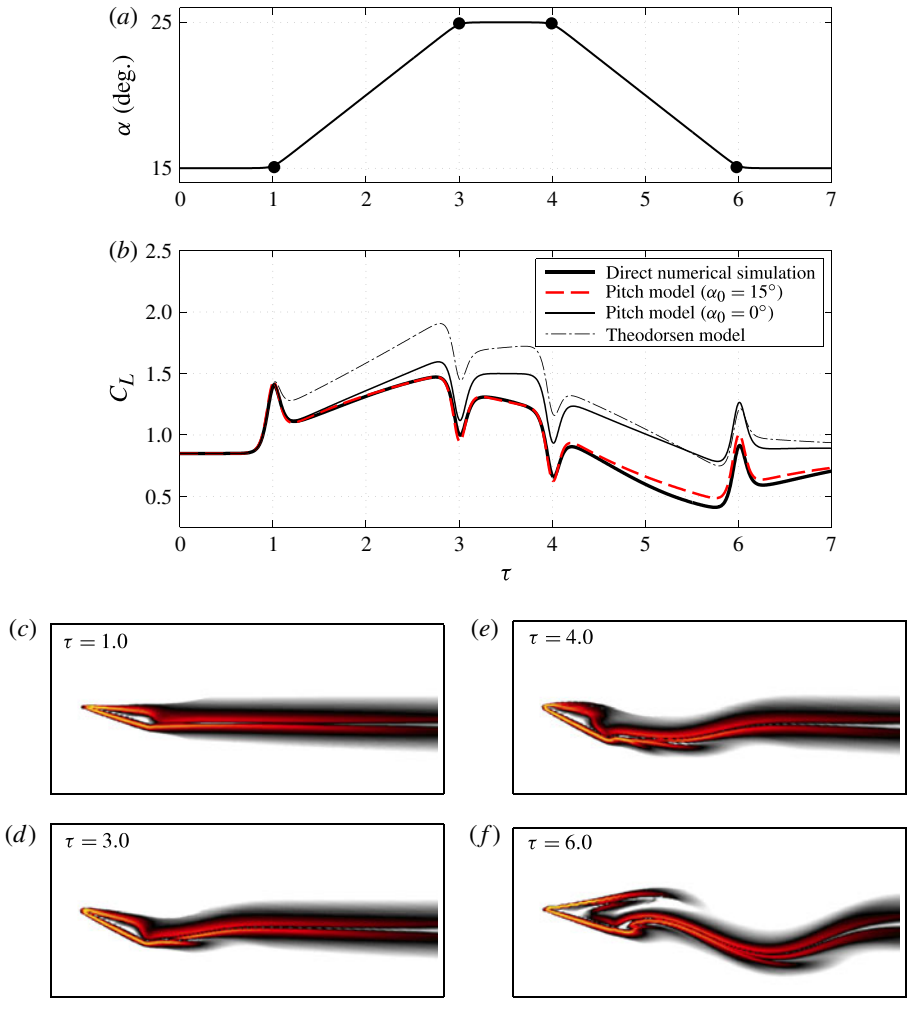


FIGURE 7. (Colour online) Improved performance of models linearized at $\alpha_0 = 15°$ over models linearized at $\alpha_0 = 0°$ for a pitch manoeuvre from 15 to 25° and back.

correct negative slope and added-mass forces at the corners. It is possible to construct a gain-scheduled or LPV model by collecting velocity field snapshots in addition to lift coefficient measurements, and synthesizing these fields into direct and pseudo-adjoint modes. These modes provide a projection from the state vector of one linearized model onto the state vector from another. However, this is the subject of future work.

Again, we note that the slope of the lift response is negative during the hold region. Investigating the FTLE field, we see that the FTLE ridge is parallel to the trailing edge at $\tau = 3.0$ and the ridge moves upstream along the upper surface of the aerofoil at $\tau = 4.0$. The trailing edge separation likely accounts for the decreased lift, despite the leading-edge vortex that typically provides enhanced lift (Taira & Colonius 2009).

This effect is more pronounced in figure 9, which shows a flat plate in a sigmoidal pitch-up manoeuvre to $\alpha = 32°$ at $Re = 300$. Because the aerofoil does not pitch back down to $\alpha = 0°$, it is possible to see the free evolution of the leading-edge vortex. Again, there is a clear difference in the high-lift and low-lift states corresponding to

https://doi.org/10.1017/jfm.2013.163 Published online by Cambridge University Press

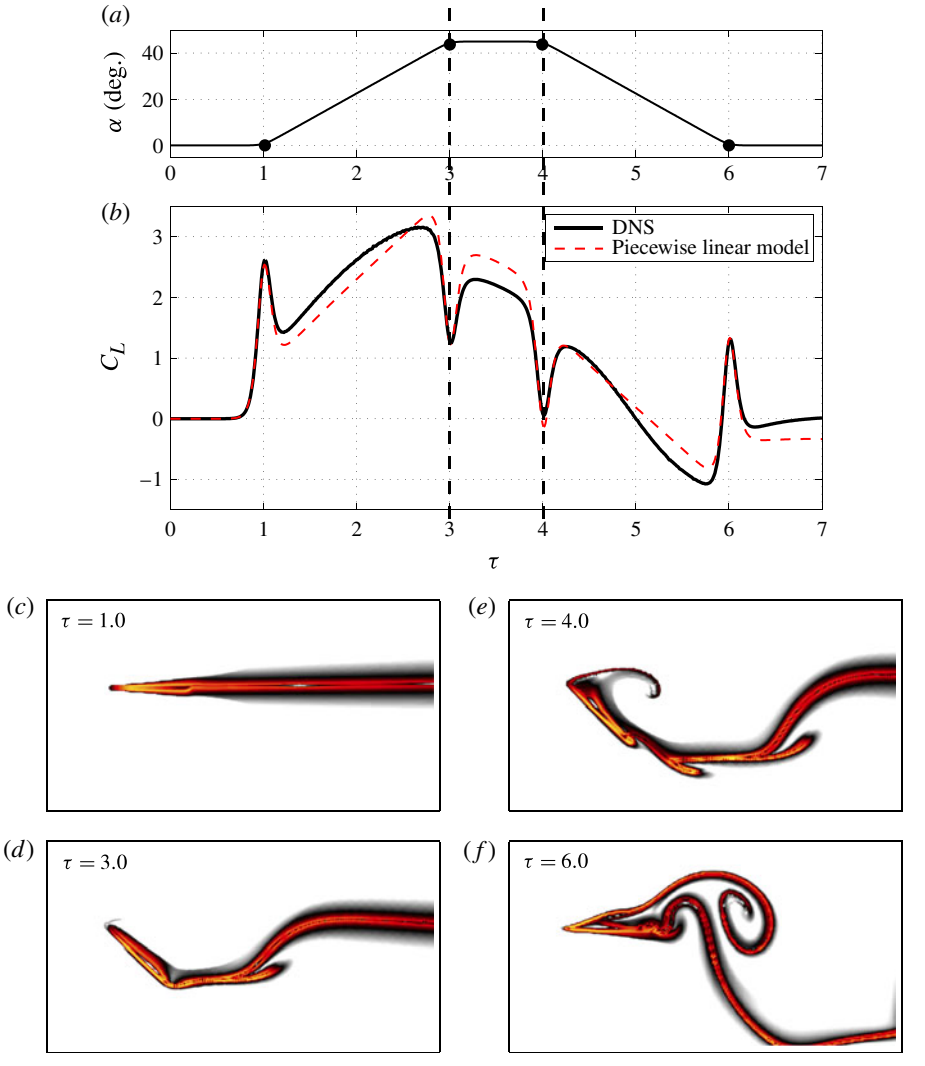


FIGURE 8. (Colour online) Comparison of the reduced-order model and DNS for a large-amplitude pitch-up, hold, pitch-down manoeuvre with a maximum angle of attack of 45°.

whether or not there is trailing-edge separation. Because this flow is at a different Reynolds number, and our linear models are not built to capture the nonlinear vortex shedding, we do not include a model comparison.

Finally, we consider an aggressive sigmoidal plunge manoeuvre in figure 10. The maximum plunging velocity corresponds to an effective angle of attack of over 40°, based on the formula $\alpha_e = \tan^{-1}(\dot{h}/U_\infty)$; however, this large effective angle of attack is short lived. The reduced-order model linearized at $\alpha_0 = 0°$ captures the lift coefficient quite well. Again, the FTLE field indicates large leading- and trailing-edge separation that convect downstream. The majority of the forces throughout the manoeuvre are added-mass forces, which appear as a doublet in the lift coefficient, contributing to the model performance.

https://doi.org/10.1017/jfm.2013.163 Published online by Cambridge University Press

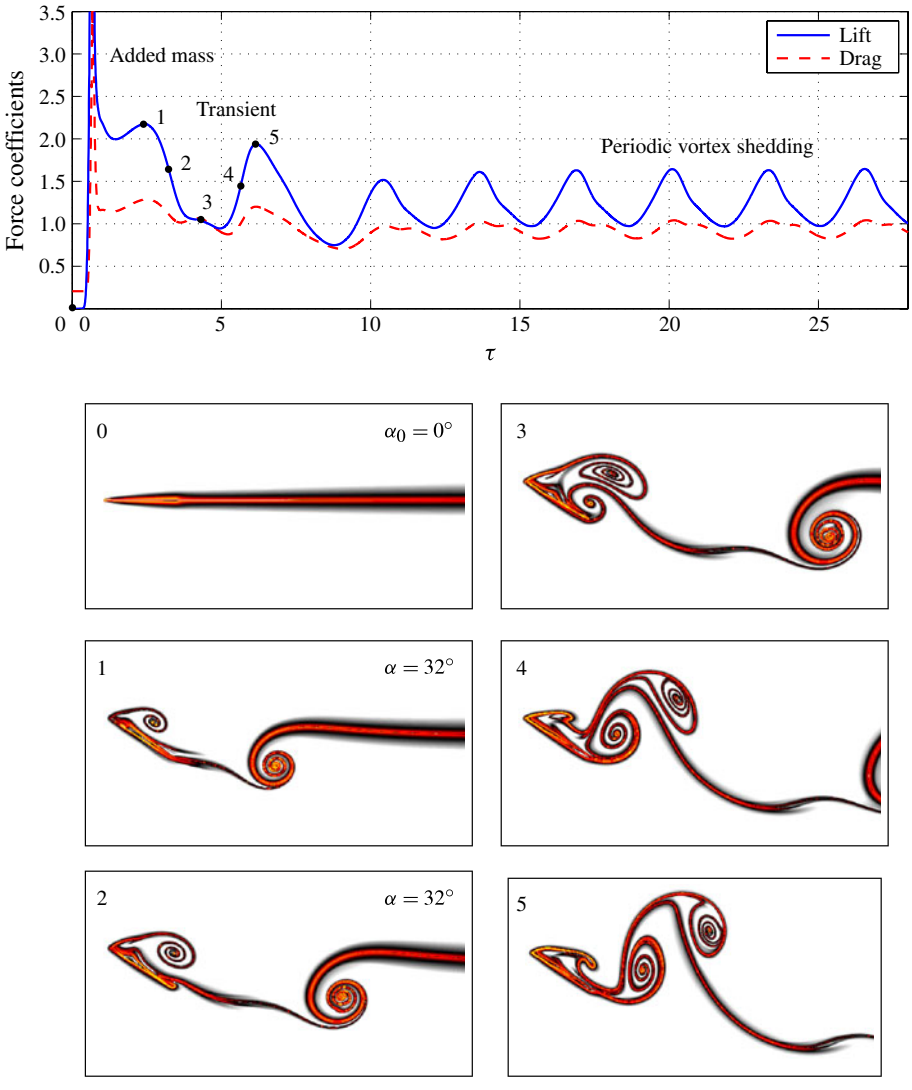


FIGURE 9. (Colour online) Flat plate aerofoil in sigmoidal pitch-up about the mid-chord from $\alpha_0 = 0°$ to $\alpha = 32°$ ($Re = 300$). Peaks in lift coefficient (1, 5) correspond to streamlined trailing-edge condition. Minima of lift coefficient (3) correspond to a trailing-edge separation point moving up towards the mid-chord of the aerofoil and strong trailing-edge roll-up.

4.6. *Summary of numerical results*

Pitch and plunge models have been developed for a flat plate at $Re = 100$ over a range of subcritical angles of attack, based on data from DNS. These models outperform Theodorsen's classical model for all motions investigated, and the performance gap widens at larger base angle of attack, as the flow becomes more separated, and the assumptions of an inviscid, planar wake become less accurate.

A number of interesting flow phenomena arise at large base angles of attack. First, as a pair of model eigenvalues moves towards the imaginary axis, the time scale for relaxation to steady-state becomes longer. In addition, at a small base angle, the

https://doi.org/10.1017/jfm.2013.163 Published online by Cambridge University Press

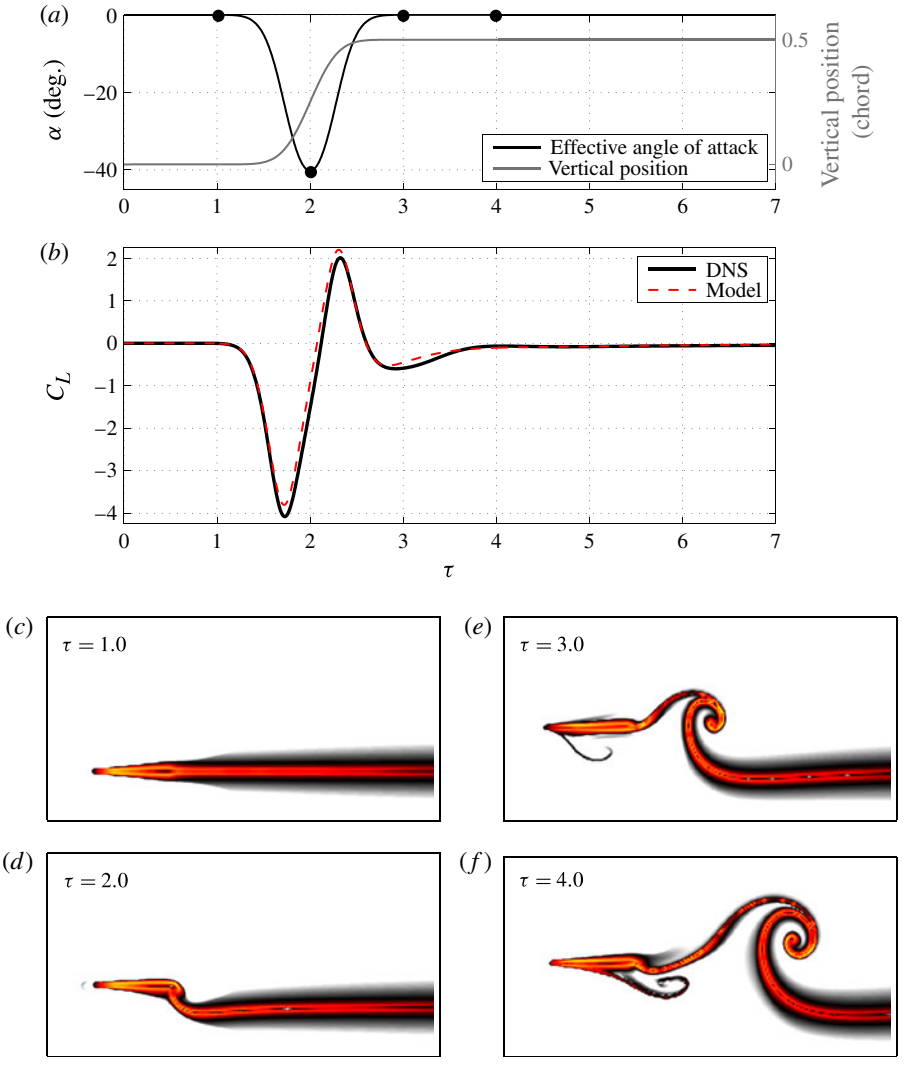


FIGURE 10. (Colour online) Comparison of the reduced-order model and DNS for a sigmoidal plunge manoeuvre. Even though there are large separated structures, and an effective angle of attack of 40°, the model agrees closely because of the large added-mass forces.

lift rises to a steady-state value after a step in the angle, and at large base angle, the lift starts at an initially high lift and decreases to steady state. The FTLE fields indicate that the flows have large separation for these manoeuvres and the lift is strongly correlated to the trailing-edge separation condition. Large lift corresponds to streamlined trailing-edge flow parallel to the plate, and low-lift states have trailing-edge separation, indicated by an FTLE ridge that moves upstream, perpendicular to the plate. The extent of the motion of the trailing-edge separation point upstream is roughly linear in the manoeuvre, so the model captures the behaviour of rapid manoeuvres past the critical bifurcation angle.

In the next section, the reduced-order models (3.4) and (3.6) and Theodorsen's model are tested at higher Reynolds numbers in wind-tunnel experiments. Instead

https://doi.org/10.1017/jfm.2013.163 Published online by Cambridge University Press

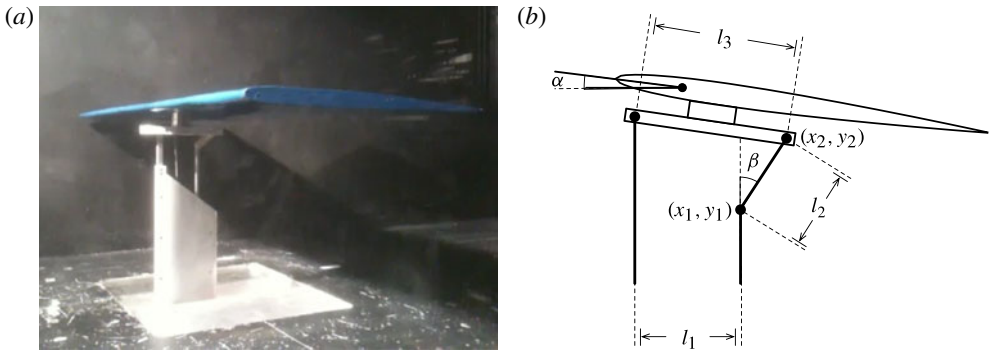


FIGURE 11. (Colour online) (*a*) NACA 0006 model in the wind tunnel. (*b*) Schematic of the hinge apparatus connecting pushrods to the platform.

of a two-dimensional flat plate, we now use a lightweight, three-dimensional NACA 0006 aerofoil with rounded leading edge; three-dimensional effects are reduced by having the aerofoil span nearly the entire width of the wind tunnel. The following experimental results at higher Reynolds number are a more realistic test of these models.

5. Experimental apparatus

The following experimental data was collected in the Andrew Fejer Unsteady Flow Wind Tunnel at the Illinois Institute of Technology. The dimensions of the wind-tunnel test section are 0.6 m × 0.6 m × 3.5 m.

The model is a NACA 0006 aerofoil, shown in figure 11(*a*), with a chord length of 0.246 m and span of 0.598 m. The free-stream velocity is 4.00 m s^{-1}, which results in a Reynolds number of approximately 65 000 and a convective time of 0.0615 s. In all pitching experiments the pitch point is at the 11 % chord location.

Forces and moments are measured using a six-axis ATI Nano17 force transducer. The free stream velocity is measured using a Pitot tube with a Validyne DP-103 pressure transducer. The model is actuated using two Copley servo tubes connected to individual pushrods, allowing for a full range of pitch and plunge motions.

The force transducer moves with the body, so forces are measured in the body-fixed frame of the aerofoil. Therefore, we rotate the normal (N) and parallel (P) forces in the z- and x-directions into the lift (L) and drag (D) forces relative to the free-stream velocity:

$$\begin{bmatrix} L \\ D \end{bmatrix} = \begin{bmatrix} \cos(\alpha) & -\sin(\alpha) \\ \sin(\alpha) & \cos(\alpha) \end{bmatrix} \begin{bmatrix} N \\ P \end{bmatrix}. \tag{5.1}$$

The lift and drag forces are then converted into non-dimensional force coefficients.

The pushrods are connected to the aerofoil and force balance via a lightweight aluminum platform with a hinge constraint, as shown in figure 11(*b*). It is possible to command an angle of attack α by varying the relative displacement of the two pushrods. For the pitching experiments below, the front pushrod is held fixed, and the height of the rear pushrod y_1 is varied to change α. The vertical displacement y_1 may

https://doi.org/10.1017/jfm.2013.163 Published online by Cambridge University Press

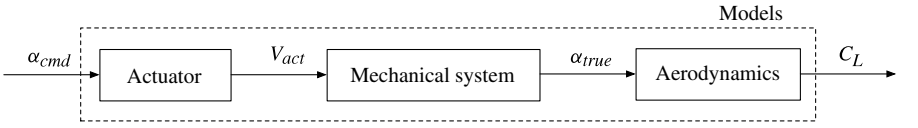


FIGURE 12. Schematic of signals in the wind-tunnel experiment. Here V_{act} is the actuator voltage.

be solved for as a function of α, and vice versa, using the following relationship:

$$(l_3\cos(\alpha) - l_1)^2 + (-l_3\sin(\alpha) - y_1)^2 - l_2^2 = 0, \tag{5.2}$$

where $l_1 = 2.1''$, $l_2 = 1.25''$ and $l_3 = 3''$ for the set-up in figure 11.

Finally, the inertia of the model, sting and pushrods introduces time lags, so the measured angle is not exactly the same as the commanded angle. In addition, the Copley servo tube controller has its own PID dynamics to track a reference position. Figure 12 is a schematic of the signals. The model input is the commanded angle of attack, α_{cmnd}, so that the models include the effect of the actuator and the mechanical apparatus.

5.1. *Phase-averaged force measurements*

To reduce the magnitude of sensor noise in the force measurements, we phase average over a number of cycles. Data is collected for N identical runs and averaged, resulting in a reduction of noise by a factor $\sqrt{N}$. Figure 13(*a,b*) shows the force measurements with sensor noise for a 5° step, and the bottom shows the phase-averaged force. In addition to strong added-mass peaks, there is a significant resonant oscillation in the phase-averaged force signal. This is investigated in the following section.

Before phase averaging, we use a sixth-order Butterworth low-pass filter at 2500 Hz. In addition, we coarsen the data by averaging the measurements inside each interval $[k\Delta t, (k+1)\Delta t)$, where $\Delta t = 0.1$ convective time unit, or 0.00615 s. Using this coarsened data as an input to the OKID method results in a discrete-time model with time step Δt. Because the high-frequency forces are dominated by added-mass, a time step of $\Delta t = 0.1$ is sufficiently small to excite and characterize the transient dynamics.

5.2. *Mechanical resonance*

Figure 14 shows the power spectrum of the normal force measurement for a number of experiments designed to isolate the source and frequency of various mechanical resonances. In one case, the bottom of the actuator assembly is struck with a rubber mallet, resulting in a strong resonance at 77 Hz and at 138 Hz. When power is fed to the servo motor controller, a significant resonant peak at 38 Hz develops, regardless of whether or not the wind-tunnel fan is on. It is likely that the resonance peak at 38 Hz is a result of the internal PID dynamics of the servo motor controller, partially explaining the peaks in the Bode plots at nearby frequencies in the following section.

6. Results: flow past a NACA0006 aerofoil at $Re = 65\,000$

Unsteady aerodynamic models are developed for a NACA 0006 aerofoil at Reynolds number 65 000 based on wind-tunnel measurements discussed in the previous section. Pitch and plunge models of the form in (3.6) are constructed using the ERA/OKID

https://doi.org/10.1017/jfm.2013.163 Published online by Cambridge University Press

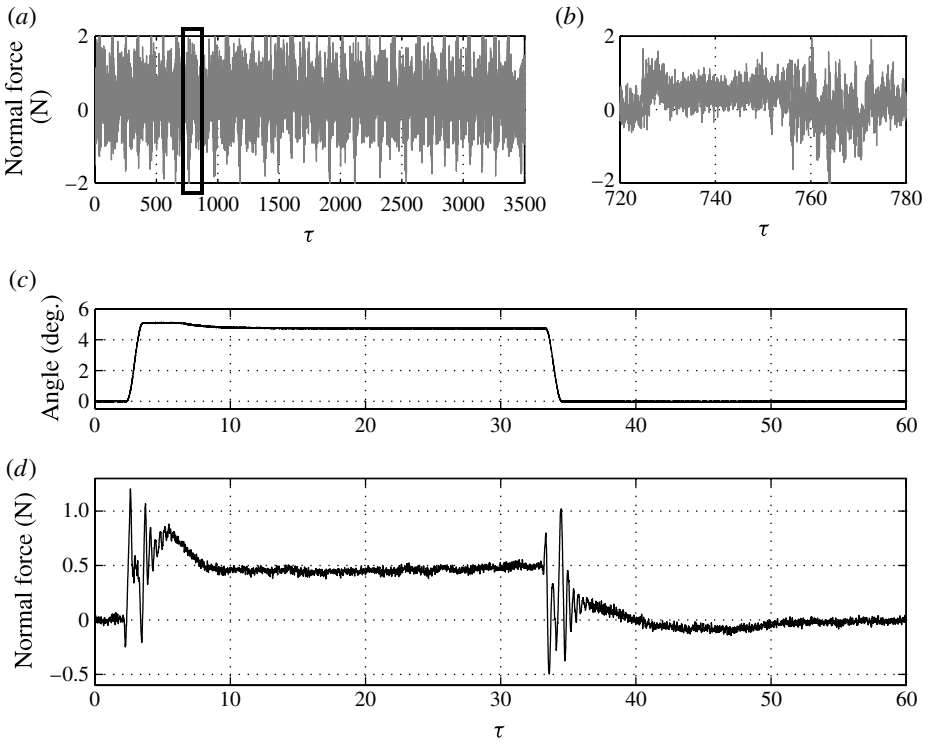


FIGURE 13. Phase-averaged force measurement for 5° step-up, step-down.

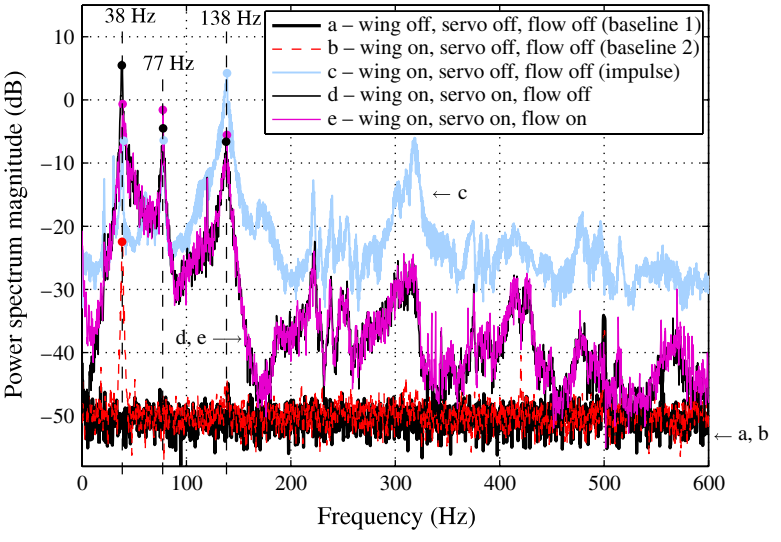


FIGURE 14. (Colour online) Mechanical resonances involved in the wind-tunnel experiment. Circles show the relative magnitudes and frequencies of the peaks of each experiment.

https://doi.org/10.1017/jfm.2013.163 Published online by Cambridge University Press

	Error (Theodorsen)	Error (ERA model)	Markov parameters	Model order
Pitch, $\alpha_0 = 0°$	0.0604	0.0331	100	7
Pitch, $\alpha_0 = 5°$	0.0752	0.0430	50	5
Pitch, $\alpha_0 = 10°$	0.1279	0.0629	150	5
Plunge, $\alpha_0 = 0°$	0.1414	0.0701	100	5
Plunge, $\alpha_0 = 10°$	0.2028	0.0991	100	5

TABLE 1. Comparison of Theodorsen and ERA model error with wind-tunnel measurements for pitch and plunge manoeuvres. Error is quantified by computing the standard deviation, from zero mean, of the error signal (measurement minus model).

method in conjunction with aggressive system identification manoeuvres described in § 3. It is shown that the low-order models identified from experiments are more accurate than Theodorsen's model for all manoeuvres, especially those based at larger angle of attack. We compute the reduced-order models using an on-design pseudo-random manoeuvre and test the performance of the models on several pseudo-random off-design manoeuvres; the model performance is similar to the on-design case, and these plots are not shown.

After identifying significant mechanical ringing and aeroelastic effects in earlier results, the structural supports were rebuilt and the PID controller was tuned to reduce sources of noise and vibration. In addition, a more sensitive Nano17 force transducer is used to measure forces, so that less aggressive manoeuvres may be accurately measured.

6.1. *Pitching experiments*

An aggressive pseudo-random manoeuvre, shown in figure 15(*a*), is used to obtain a reduced-order model of the form in (3.6) for pitching motion linearized about $\alpha_0 = 0°$. Figure 15(*b*) shows the measured and modelled response. Both models, (3.6) and Theodorsen's model, appear to closely match the measured force; however, from table 1 in § 6.3, Theodorsen's model has nearly twice the error as the ERA model. The agreement with Theodorsen's model at $\alpha_0 = 0°$ speaks to the accuracy of the experiments after mechanical resonances were isolated and removed.

Figure 16 shows the same pitch manoeuvre performed at a base angle of $\alpha_0 = 10°$. For this manoeuvre, Theodorsen's model is significantly less accurate than in the $\alpha_0 = 0°$ case. This is not entirely surprising, considering that the flow physics is increasingly complex for larger angles of attack. In addition, the behaviour in the hold regions is qualitatively different from the $\alpha_0 = 0°$ case: instead of a transient rise to the steady-state value, the lift starts at an initially high value at the beginning of the hold, and decreases to the steady-state value. Similar behaviour was observed in simulations, where the difference in behaviour was explained by leading-edge and trailing-edge separation, as in figure 7.

Figure 17 compares the Bode plots of the ERA models at $\alpha_0 = 0°$ and $\alpha_0 = 10°$ and Theodorsen's model. The model linearized at $\alpha_0 = 10°$ converges to the low-frequency asymptote at a lower frequency than the $\alpha_0 = 0°$ model, and the magnitude is smaller at low frequencies, consistent with a decreased lift coefficient slope. In addition, since these models include the effect of the actuator and mechanical system, there is a strong mechanical resonance at 30 rad s^{-1} c U^{-1}, which corresponds to ~76 Hz. The model at $\alpha_0 = 10°$ does not have a prominent resonance at 11 rad s^{-1} c U^{-1} (28 Hz),

https://doi.org/10.1017/jfm.2013.163 Published online by Cambridge University Press

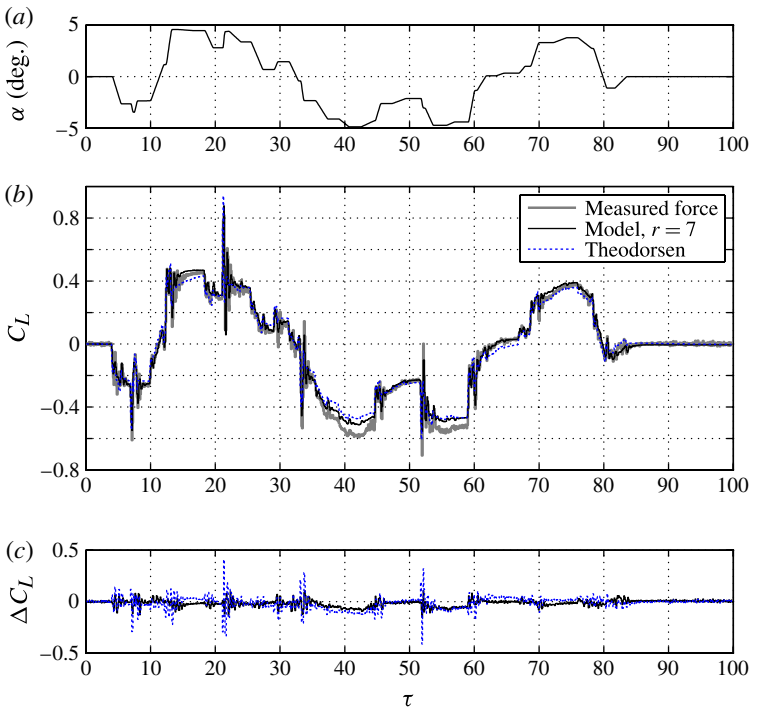


FIGURE 15. (Colour online) Experimental and modelled lift for pitch about a base angle $\alpha_0 = 0°$.

unlike the model based at $\alpha_0 = 0°$. It appears that the boundary-layer separation at $\alpha_0 = 10°$ has almost entirely eliminated this resonance.

6.2. *Plunge experiments*

An aggressive plunge manoeuvre can be seen in figure 18(*a*). Since the C_h term is zero in the plunge model (3.6), it is unnecessary to have the hold portions of the manoeuvre at different heights. Therefore, the new manoeuvre accelerates into linear ramps of different vertical velocity until a maximum or minimum height has been reached, after which the position is held for a time and then the direction is reversed. The different vertical velocities correspond to different effective angles of attack.

Figure 18 shows the results for plunging at $\alpha_0 = 0°$ and figure 19 shows the results for plunging about $\alpha_0 = 10°$. At $\alpha_0 = 0°$ Theodorsen's model is quite accurate, capturing the qualitative behaviour. At $\alpha_0 = 10°$, however, Theodorsen's model fails to predict the regions of constant vertical velocity, which correspond to a constant effective angle of attack. In fact, during these effective angle of attack holds, Theodorsen's model rises to a steady state that is larger in magnitude, while the actual lift decreases from a large initial value. Although the reduced-order model is more accurate at capturing this phenomena, it is clear from the error signal that both models systematically under-predict the lift at the beginning of these hold periods.

6.3. *Model benchmarks*

The results of §§ 6.1 and 6.2 are summarized here. Table 1 shows the error between the measured data and both Theodorsen's model and the identified model, (3.6) from

https://doi.org/10.1017/jfm.2013.163 Published online by Cambridge University Press

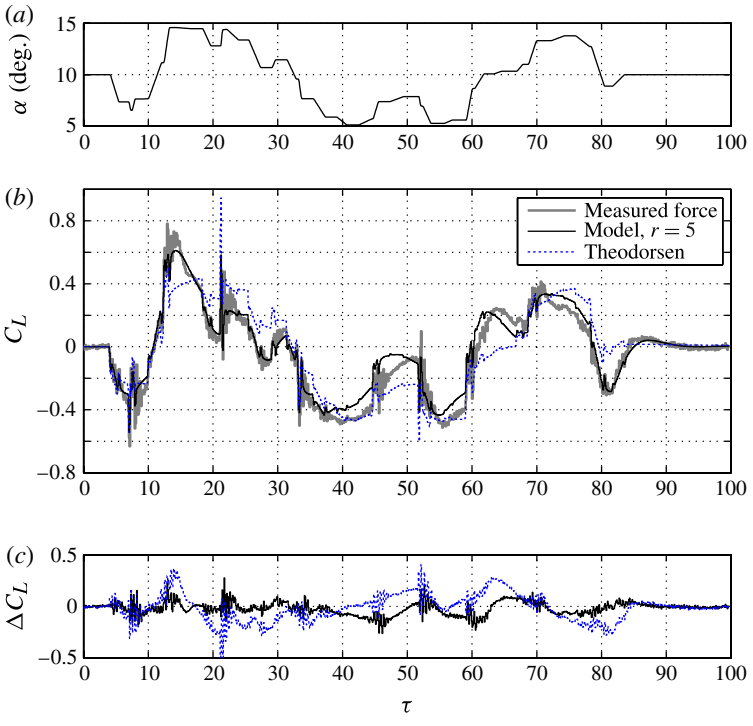


FIGURE 16. (Colour online) Experimental and modelled lift for pitch about a base angle $\alpha_0 = 10°$.

ERA/OKID. The error is measured by integrating the square of the difference between each model and the measured data for a given manoeuvre. In each case, the error in the ERA model is about half of the error in Theodorsen's model. The error increases with the base angle of attack, α_0, which is reasonable, since the flow becomes increasingly nonlinear for increasing angle of attack. The number of Markov parameters (values of the discrete-time impulse response from OKID used by ERA) is reported.

The inherent time delay between command signal and measured force is identified by choosing the time delay that minimizes the model error for the case of pitching about $\alpha_0 = 0°$. The results are shown in table 2. Recall from § 5.1 that the coarse sample time is $\Delta t = 0.1$ convective time units. Since the error is the same for a time delay of $2\Delta t$ and $3\Delta t$, it helps to use other indicators, such as the frequency response or how closely the peaks in $\ddot{\alpha}$ line up with the added-mass peaks in the force measurement. Based on these comparisons, it was determined that the time delay is $\tau_d = 3\Delta t$ (0.3 convective times). This imposes a fundamental bandwidth limitation for closed-loop feedback control of $1/\tau_d$ rad s^{-1} c U^{-1}, which is 8.6 Hz in dimensional units. This bandwidth is higher than was reported by Kerstens *et al.* (2011) using leading-edge actuation.

6.4. *Discussion about experimental results*

Reduced-order models for the unsteady lift force have been obtained from wind-tunnel measurements of a pitching and plunging aerofoil. The wind tunnel is a more challenging test case with the addition of flow disturbances, time delays and

https://doi.org/10.1017/jfm.2013.163 Published online by Cambridge University Press

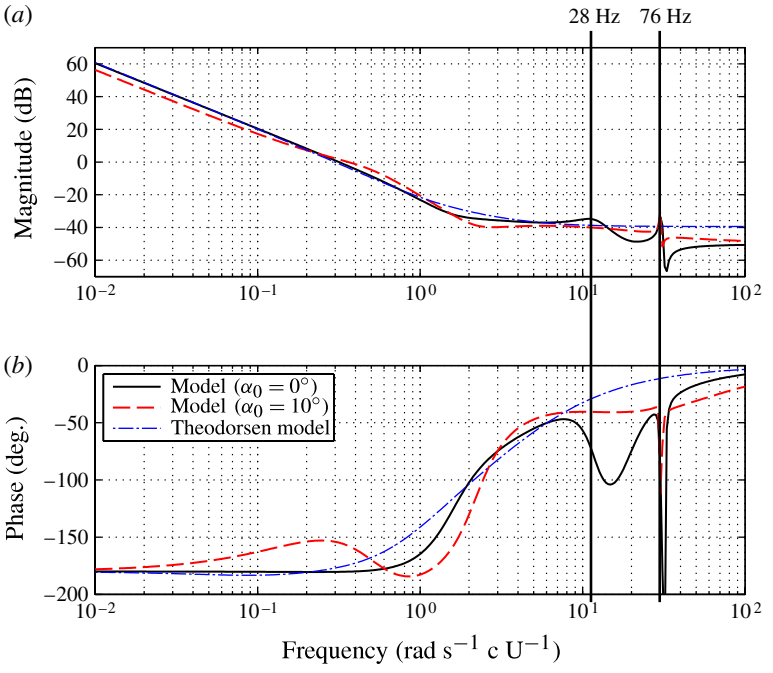


FIGURE 17. (Colour online) Bode plots of pitch models at $\alpha_0 = 0°$ and $\alpha_0 = 10°$. Pitch is ∼11 % chord.

Model order	7	7	7	7
Time delay (Δt)	1	2	3	4
Error (ERA model)	0.0359	0.0331	0.0331	0.0727

TABLE 2. Effect of assumed time delay on model error. The model is the $\alpha_0 = 0°$ pitch case. A total of 100 Markov parameters are used with $\Delta t = 0.1$ convective time units.

sensor noise. In addition, the experiment is performed at a moderate Reynolds number, $Re = 65\,000$, with a three-dimensional wing with rounded leading edge, providing a more realistic model of a MAV. The issue of plant disturbance and sensor noise motivates the use of aggressive manoeuvres, which excite strong unsteady aerodynamic responses across a range of relevant frequencies. These manoeuvres are used in conjunction with the ERA/OKID algorithm to construct pitch and plunge models of the form in (3.6).

In both pitch and plunge experiments, at $\alpha_0 = 0°$ and $\alpha_0 = 10°$, the reduced-order model outperforms Theodorsen's model. At larger base angle of attack, $\alpha_0 = 10°$, the difference with Theodorsen is more pronounced. At $\alpha_0 = 10°$ both models have larger total error than in the $\alpha_0 = 0°$ case, because of nonlinear flow effects that are not modelled. The fact that the low-order model captures the additional mechanical effects indicates that these methods may be applied more generally to problems in aeroelasticity. There is also an aerodynamic cushioning effect at $\alpha_0 = 10°$, whereby the mechanical resonance is attenuated and occurs at a slightly higher frequency.

https://doi.org/10.1017/jfm.2013.163 Published online by Cambridge University Press

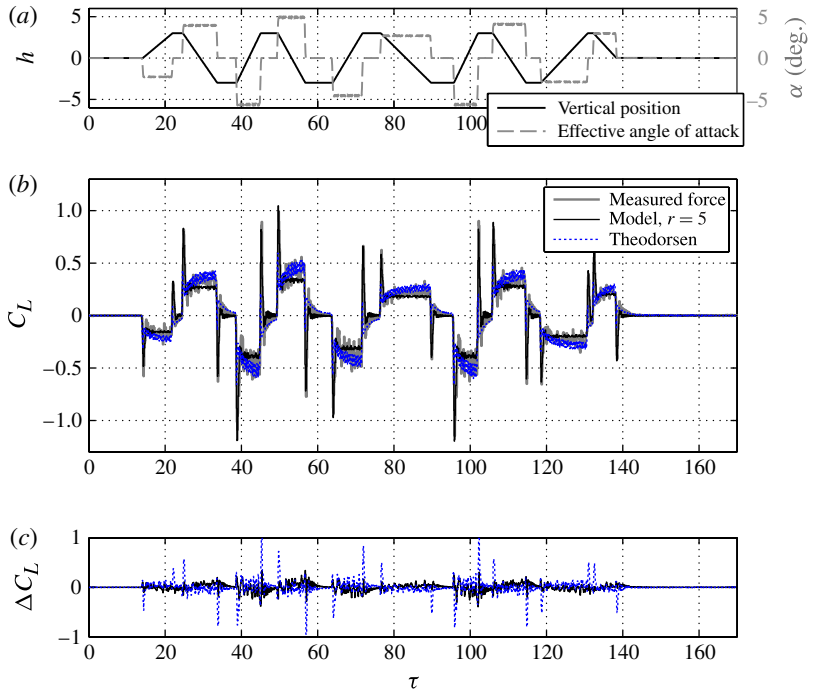


FIGURE 18. (Colour online) Experimental and modelled lift for plunge about a base angle of $\alpha_0 = 0°$.

The models based on wind-tunnel measurements follow similar trends to those based on simulations. For example, at larger base angle of attack, the model takes longer to equilibrate to steady state, as reflected in the convergence to the quasi-steady asymptote at a lower frequency. In addition, at $\alpha_0 = 0°$, the data and models exhibit a transient rise to their steady-state values given a step in effective angle of attack, while at $\alpha_0 = 10°$, the data and models exhibit a transient decay to their steady-state values from a larger initial value. In simulations, this is due to leading-edge and trailing-edge separation.

7. Conclusions and discussion

In this work, we have developed reduced-order models, and a flexible modelling procedure, for the unsteady pitching and plunging aerodynamics of two low-Reynolds-number configurations. The first set of results are two-dimensional DNS of a flat plate at $Re = 100$. It is shown that for a relatively low-order model, with order $r = 7$, the unsteady aerodynamic effects are well captured for all angles of attack up to the Hopf bifurcation angle. The second set of results are based on wind-tunnel measurements of a NACA 0006 aerofoil at $Re = 65\,000$. These experiments motivated the development of aggressive system identification manoeuvres for use with the OKID method, which allows for accurate system identification over a range of frequencies, despite the reduced signal-to-noise ratio experienced in high-reduced-frequency, low-Reynolds-number wind-tunnel experiments. The modelling procedure is able to capture the additional dynamics associated with the structural resonance and actuator dynamics in the experiment.

https://doi.org/10.1017/jfm.2013.163 Published online by Cambridge University Press

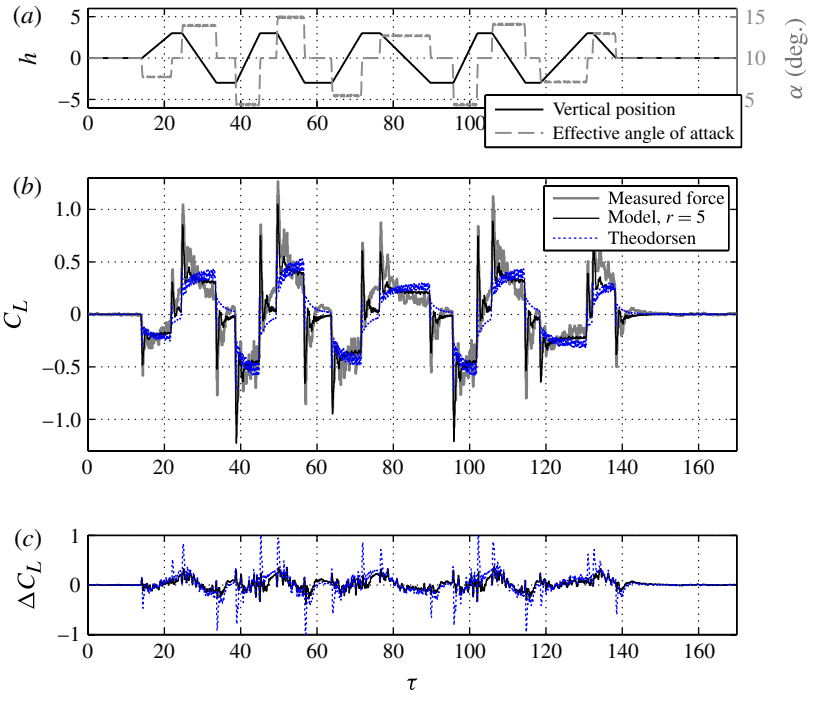


FIGURE 19. (Colour online) Experimental and modelled lift for plunge about a base angle of $\alpha_0 = 10°$.

The models presented in this paper provide quantifiable insights into the physics of laminar separation that characterize flows at low Reynolds number. In both the simulated results and the wind-tunnel measurements, the low-order models exhibit similar trends as the angle of attack is increased. The quasi-steady model asymptote is pushed to lower frequencies at larger base angle of attack, α_0, consistent with the fact that the boundary layer is becoming more separated and a pair of complex eigenvalues moves toward the imaginary axis in the models. In addition, we observe that poles and zeros of the reduced-order models approach the imaginary axis as the base angle of attack is increased, and at a subcritical angle of attack, some zeros move into the right half-plane. This has significant consequences for feedback control; in particular, the introduction of zeros in the right half-complex-plane will impose fundamental limitations on the bandwidth that may be achieved with closed-loop feedback control (Kerstens *et al.* 2011). In the experiment, we see an attenuation of the structural resonance at large angle of attack, due to the cushioning effect of the separated boundary layer. In both simulations and experiments, it is observed that there is qualitatively different behaviour at low and high base angle of attack for the lift in response to a step-up in angle of attack: at low angle of attack, the lift rises to the steady-state value, whereas at high angle of attack, the lift decreases to the steady-state value from an initial high lift state. This suggests the formation of a leading-edge vortex, followed by trailing-edge separation at large angles of attack, which is confirmed using FTLE visualizations.

An important feature of this study is the determination of flow regimes where these models start to break down. Because the models are reduced-order models of the

https://doi.org/10.1017/jfm.2013.163 Published online by Cambridge University Press

linearized discrete NS equations with lift output equation, it is expected that they will not be valid for flows that are dominated by nonlinear phenomena, such as vortex shedding or large leading-edge vortex formation. For example, the models are not necessarily valid when the angle of attack, α, or the effective angle of attack, α_e, based on the Strouhal number, exceeds the critical angle of attack at which Hopf bifurcation occurs. As the base angle of attack approaches this critical angle, the radius of validity of the model shrinks. However, it was demonstrated on several large-amplitude manoeuvres, in which the flow was massively separated, that the model does surprisingly well, as long as there are large angular or vertical rates associated with the motion, resulting in added mass.

The models developed here will be particularly useful in the context of active flow control. The low-dimensional state-space form of these models is ideal for use with modern control techniques, such as $\mathscr{H}_2$ and $\mathscr{H}_\infty$ synthesis (Kim & Bewley 2007; Bagheri *et al.* 2009; Ahuja & Rowley 2010). In particular, the authors envision an experimental demonstration of robust lift control that tracks a specified reference lift while rejecting gust disturbances and attenuating sensor noise. As the base angle of attack is increased and zeros enter the right half plane, there will be fundamental limitations on the bandwidth of the closed-loop system. The design of flight controllers for MAVs is challenging, since the flight dynamic and fluid dynamic time scales are comparable. The typical control paradigm of inner-loop/outer-loop design will no longer yield robust controllers, and it will become necessary to apply modern control techniques. This is the focus of current work by the authors.

Acknowledgements

The authors gratefully acknowledge the support for this work from the Air Force Office of Scientific Research grant FA9550-12-1-0075, and by the FAA, under the Joint University Program. We also thank W. Kerstens, J. Eldredge, M. Ol and the AIAA fluid dynamics technical committee's low-Reynolds-number aerodynamics discussion group. Finally, we would like to thank the anonymous referees for valuable comments.

REFERENCES

AHUJA, S. & ROWLEY, C. W. 2010 Feedback control of unstable steady states of flow past a flat plate using reduced-order estimators. *J. Fluid Mech.* **645**, 447–478.

ANDERSON, J. M., STREITLIEN, K., BARRETT, D. S. & TRIANTAFYLLOU, M. S. 1998 Oscillating foils of high propulsive efficiency. *J. Fluid Mech.* **360**, 41–72.

APKARIAN, P., PELLANDA, P. & TUAN, H. D. 2000 Mixed h_2/h_∞ multi-channel linear parameter-varying control in discrete time. *Syst. Control Lett.* **41**, 333–346.

BAGHERI, S., BRANDT, L. & HENNINGSON, D. S. 2009 Input–output analysis, model reduction and control of the flat-plate boundary layer. *J. Fluid Mech.* **620**, 263–298.

BAMIEH, B. & GIARRÉ, L. 2002 Identification of linear parameter varying models. *Intl J. Robust Nonlinear Control* **12**, 841–853.

BIRCH, J. & DICKINSON, M. 2001 Spanwise flow and the attachment of the leading-edge vortex on insect wings. *Nature* **412**, 729–733.

BRENNEN, C. E. 1982 A review of added mass and fluid inertial forces. *Tech. Rep.* CR 82.010. Naval Civil Engineering Laboratory.

BRUNTON, S. L. 2012 Unsteady aerodynamic models for agile flight at low Reynolds numbers. PhD thesis, Princeton University.

BRUNTON, S. L. & ROWLEY, C. W. 2010 Fast computation of FTLE fields for unsteady flows: a comparison of methods. *Chaos* **20**, 017503.

https://doi.org/10.1017/jfm.2013.163 Published online by Cambridge University Press

BRUNTON, S. L. & ROWLEY, C. W. 2013 Empirical state-space representations for Theodorsen's lift model. *J. Fluids Struct.* **38**, 174–186.

BUCHHOLZ, J. H. J. & SMITS, A. J. 2008 The wake structure and thrust performance of a rigid, low-aspect-ratio pitching panel. *J. Fluid Mech.* **603**, 331–365.

COLONIUS, T. & TAIRA, K. 2008 A fast immersed boundary method using a nullspace approach and multi-domain far-field boundary conditions. *Comput. Meth. Appl. Mech. Engng* **197**, 2131–2146.

DANIEL, T. L. 1984 Unsteady aspects of aquatic locomotion. *Am. Zool.* **24** (1), 121–134.

DULLERUD, G. E. & PAGANINI, F. 2000 *A Course in Robust Control Theory: A Convex Approach*. Springer.

EDWARDS, J. W. 1977 *Unsteady Aerodynamic Modeling and Active Aeroelastic Control. SUDARR 504*. Stanford University.

ELDREDGE, J. D., WANG, C. & OL, M. V. 2009 A computational study of a canonical pitch-up, pitch-down wing maneuver. *AIAA Paper* 2009-3687, 39th Fluid Dynamics Conference.

FRANCO, E., PEKAREK, D. N., PENG, J. & DABIRI, J. O. 2007 Geometry of unsteady fluid transport during fluid–structure interactions. *J. Fluid Mech.* **589**, 125–145.

GREEN, M. A., ROWLEY, C. W. & HALLER, G. 2007 Detection of Lagrangian coherent structures in 3D turbulence. *J. Fluid Mech.* **572**, 111–120.

GREEN, M. A., ROWLEY, C. W. & SMITS, A. J. 2011 The unsteady three-dimensional wake produced by a trapezoidal pitching panel. *J. Fluid Mech.* **685**, 117–145.

GREEN, M. A. & SMITS, A. J. 2008 Effects of three-dimensionality on thrust production by a pitching panel. *J. Fluid Mech.* **615**, 211–220.

HALLER, G. 2002 Lagrangian coherent structures from approximate velocity data. *Phys. Fluids* **14** (6), 1851–1861.

HALLER, G. 2004 Exact theory of unsteady separation for two-dimensional flows. *J. Fluid Mech.* **512**, 257–311.

ILAK, M. & ROWLEY, C. W. 2008 Modeling of transitional channel flow using balanced proper orthogonal decomposition. *Phys. Fluids* **20**, 034103.

ILLINGWORTH, S. J., MORGANS, A. S. & ROWLEY, C. W. 2010 Feedback control of flow resonances using balanced reduced-order models. *J. Sound Vib.* **330** (8), 1567–1581.

JUANG, J. N. & PAPPA, R. S. 1985 An eigensystem realization algorithm for modal parameter identification and model reduction. *J. Guid. Control Dyn.* **8** (5), 620–627.

JUANG, J. N., PHAN, M., HORTA, L. G. & LONGMAN, R. W. 1991 Identification of observer/Kalman filter Markov parameters: theory and experiments. Technical Memorandum 104069. NASA.

KAPLAN, S. M., ALTMAN, A. & OL, M. 2007 Wake vorticity measurements for low aspect ratio wings at low Reynolds number. *J. Aircraft* **44** (1), 241–251.

VON KÁRMÁN, T. & SEARS, W. R. 1938 Airfoil theory for non-uniform motion. *J. Aeronaut. Sci.* **5** (10), 379–390.

KERSTENS, W., PFEIFFER, J., WILLIAMS, D., KING, R. & COLONIUS, T. 2011 Closed-loop control of lift for longitudinal gust suppression at low Reynolds numbers. *AIAA J.* **49** (8), 1721–1728.

KIM, J. & BEWLEY, T. R. 2007 A linear systems approach to flow control. *Annu. Rev. Fluid Mech.* **39**, 383–417.

LESIEUTRE, D. J., REISENTHEL, P. H. & DILLENIUS, M. F. E. 1994 A practical approach for calculating aerodynamic indicial functions with a Navier–Stokes solver. *AIAA Paper* 94-0059, 32nd Aerospace Sciences Meeting.

LJUNG, L. 1999 *System Identification: Theory for the User*. Prentice Hall.

MA, Z., AHUJA, S. & ROWLEY, C. W. 2011 Reduced order models for control of fluids using the eigensystem realization algorithm. *Theor. Comput. Fluid Dyn.* **25** (1), 233–247.

OL, M. V., ALTMAN, A., ELDREDGE, J. D., GARMANN, D. J. & LIAN, Y. 2010 Résumé of the AIAA FDTC low Reynolds number discussion group's canaonical cases. *AIAA Paper* 2010-1085, 48th Aerospace Sciences Meeting.

https://doi.org/10.1017/jfm.2013.163 Published online by Cambridge University Press

OR, A. C. & SPEYER, J. L. 2010 Empirical pseudo-balanced model reduction and feedback control of weakly nonlinear convection patterns. *J. Fluid Mech.* **662**, 36–65.

PENG, J. & DABIRI, J. O. 2008 The 'upstream wake' of swimming and flying animals and its correlation with propulsive efficiency. *J. Expl Biol.* **211**, 2669–2677.

PINES, D. J. & BOHORQUEZ, F. 2006 Challenges facing future micro-air-vehicle development. *J. Aircraft* **43** (2), 290–305.

PULLIN, D. I. & WANG, Z. J. 2004 Unsteady forces on an accelerating plate and application to hovering insect flight. *J. Fluid Mech.* **509**, 1–21.

ROWLEY, C. W. 2005 Model reduction for fluids using balanced proper orthogonal decomposition. *Intl J. Bifurcation Chaos* **15** (3), 997–1013.

RUELLE, D. & TAKENS, F. 1971 On the nature of turbulence. *Commun. Math. Phys.* **20**, 167–192.

SANE, S. P. 2003 The aerodynamics of insect flight. *J. Expl Biol.* **206** (23), 4191–4208.

SHADDEN, S. C., KATIJA, K., ROSENFELD, M., MARSDEN, J. E. & DABIRI, J. O. 2007 Transport and stirring induced by vortex formation. *J. Fluid Mech.* **593**, 315–331.

SHADDEN, S. C., LEKIEN, F. & MARSDEN, J. E. 2005 Definition and properties of Lagrangian coherent structures from finite-time Lyapunov exponents in two-dimensional aperiodic flows. *Physica* D **212**, 271–304.

SURANA, A., GRUNBERG, O. & HALLER, G. 2006 Exact theory of three-dimensional flow separation. Part 1. Steady separation. *J. Fluid Mech.* **564**, 57–103.

TAIRA, K. & COLONIUS, T. 2007 The immersed boundary method: a projection approach. *J. Comput. Phys.* **225** (2), 2118–2137.

TAIRA, K. & COLONIUS, T. 2009 Three-dimensional flows around low-aspect-ratio flat-plate wings at low Reynolds numbers. *J. Fluid Mech.* **623**, 187–207.

THEODORSEN, T. 1935 General theory of aerodynamic instability and the mechanism of flutter. *Tech. Rep.* 496. NACA.

TORRES, G. E. & MUELLER, T. J. 2004 Low-aspect-ratio wing aerodynamics at low Reynolds numbers. *AIAA J.* **42** (5), 865–873.

TRIANTAFYLLOU, G. S., TRIANTAFYLLOU, M. S. & GROSENBAUGH, M. A. 1993 Optimal thrust development in oscillating foils with application to fish propulsion. *J. Fluids Struct.* **7**, 205–224.

TRUONG, K. V. & TOBAK, M. 1990 Indicial response approach derived from Navier–Stokes equations. Part 1. Time-invariant equilibrium state. Technical Memorandum 102856. NASA.

VIDELER, J. J., SAMHUIS, E. J. & POVEL, G. D. E. 2004 Leading-edge vortex lifts swifts. *Science* **306**, 1960–1962.

WAGNER, H. 1925 Über die Entstehung des dynamischen Auftriebes von Tragflügeln. *Z. Angew. Math. Mech.* **5** (1), 17–35.

WANG, Z. J. 2005 Dissecting insect flight. *Annu. Rev. Fluid Mech.* **37**, 183–210.

WELDON, M., PEACOCK, T., JACOBS, G. B., HELU, M. & HALLER, G. 2008 Experimental and numerical investigation of the kinematic theory of unsteady separation. *J. Fluid Mech.* **611**, 1–11.

WILSON, M. M., PENG, J., DABIRI, J. O. & ELDREDGE, J. D. 2009 Lagrangian coherent structures in low Reynolds number swimming. *J. Phys. C: Matt.* **21** (20), 204105.

ZBIKOWSKI, R. 2002 On aerodynamic modelling of an insect-like flapping wing in hover for micro air vehicles. *Phil. Trans. R. Soc.* A **360**, 273–290.

https://doi.org/10.1017/jfm.2013.163 Published online by Cambridge University Press